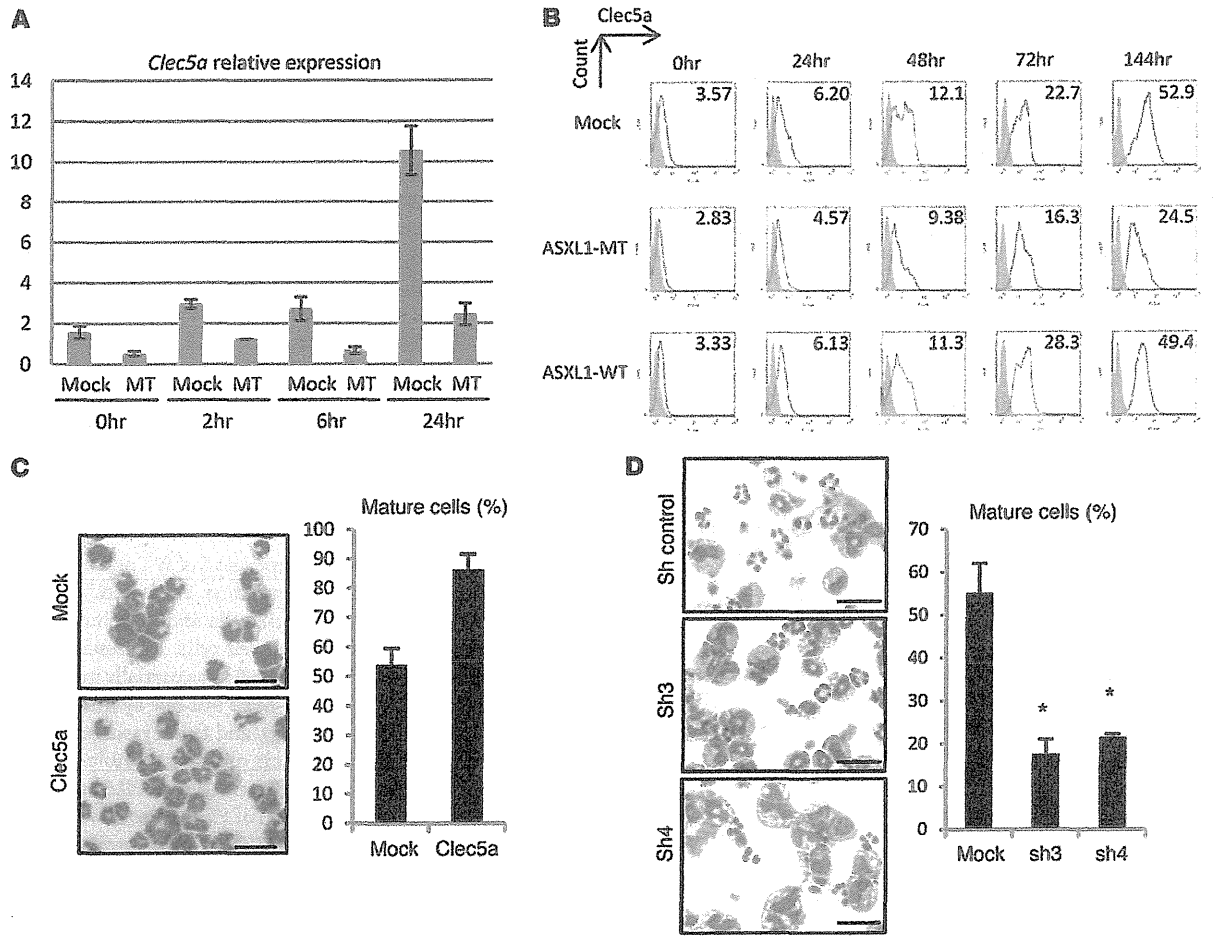

Figure 2

ASXL1 mutations reduced the expression of *Clec5a*, which contributed to the differentiation of 32Dcl3 cells. (**A**) qRT-PCR for *Clec5a* in 32Dcl3 cells transduced with pMYs-IG (mock) or pMYs-FLAG-ASXL1-MT2-IG (MT). Relative expression levels normalized by *Gapdh* mRNA were measured at the indicated time points after incubation with G-CSF (50 ng/ml). (**B**) Surface expression of Clec5a in 32Dcl3 cells transduced with mock, ASXL1-MT2 (MT), or ASXL1-WT after incubation with 50 ng/ml G-CSF. Cells were analyzed by flow cytometry at the indicated time points. MFIs are indicated. Filled histograms show control (IgG). (**C**) Left: Overexpression of *Clec5a* promoted the differentiation of HL60 cells. Morphology of HL60 cells expressing pMYs-IP (mock; top) and pMYs-Clec5a-IP (Clec5a; bottom) after incubation with 10^{-6} M ATRA for 3 days. Scale bars: 20 μm. Right: Proportion of segmented cells. (**D**) 32Dcl3 cells with or without shRNA for *Clec5a* were incubated with 50 ng/ml G-CSF for 6 days. Morphology (left) and proportion of differentiated 32Dcl3 cells (right) are shown. Scale bars: 20 μm. *$P < 0.05$. Sh control, control scramble shRNA.

Supplemental Figure 3A), suggesting that Clec5a plays a direct role in the differentiation of myeloid cells.

To examine the direct involvement of Clec5a in G-CSF–induced differentiation of 32Dcl3 cells, we designed 2 shRNAs (sh3 and sh4) for *Clec5a*, which efficiently knocked down Clec5a expression in 32Dcl3 cells (Supplemental Figure 3, B and C). Intriguingly, G-CSF–induced differentiation of 32Dcl3 was significantly inhibited by Clec5a knockdown (Figure 2D), suggesting that ASXL1-MT inhibits differentiation of 32Dcl3 cells, at least in part through suppression of Clec5a. Importantly, ectopic expression of Clec5a in ASXL1-MT–expressing 32Dcl3 cells restored the differentiation ability of 32Dcl3, although this restoration was not induced by a mutant Clec5a that harbors a K16A mutation in the transmembrane domain, which disrupts the ability to associate with DAP12 (data not shown), an activating adaptor for Clec5a that transmits the positive signal associating with Clec5a (Figure 3, A and B, Supplemental Figure 3D, and ref. 20). Thus, ASXL1-MT reduced the expression of Clec5a, which contributes to granulocytic differentiation of 32Dcl3 cells, leading to the disturbed differentiation of 32Dcl3 cells. Interestingly, expression of *CLEC5A* was reduced in the whole BM cells of the majority of patients with MDS when compared with normal BM cells (Figure 3C). However, the presence or absence of *ASXL1* mutations did not correlate with *CLEC5A* expression in BM cells of MDS patients, suggesting that other MDS disease alleles can alter *CLEC5A* expression in patients with *ASXL1*-WT.

ASXL1-MTs induced MDS-like disease in mice. Using a mouse BM transplant (BMT) model, we next examined the in vivo effect of ASXL1-MT expression. BM cells derived from 5-fluorouracil–treated Ly5.2 mice were transduced with a retrovirus vector

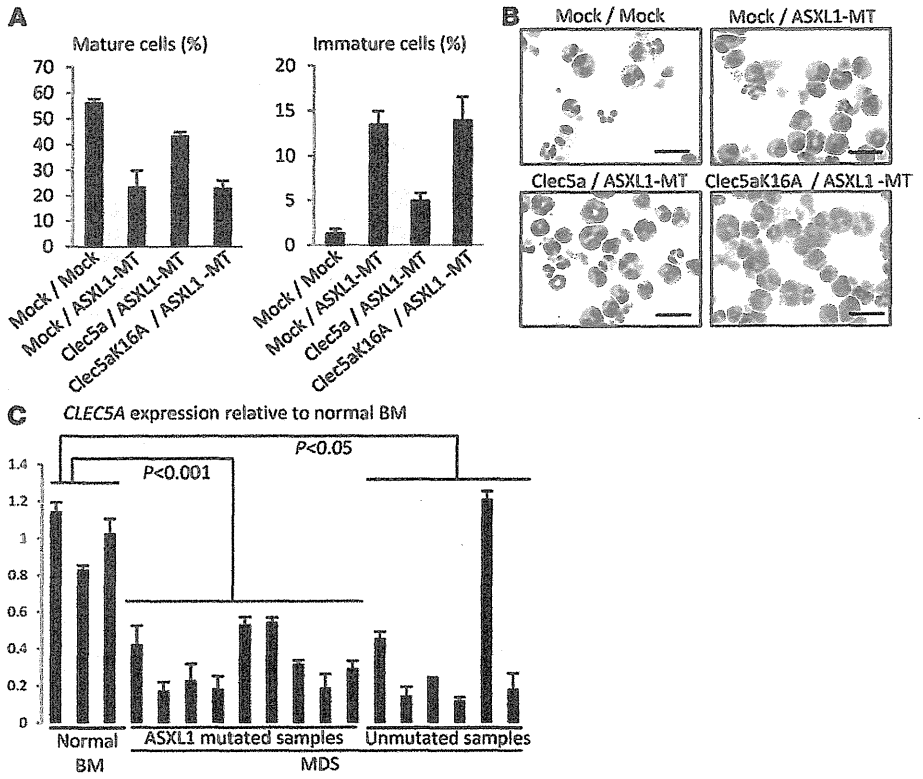

Figure 3
Downregulation of Clec5a caused by ASXL1-MT played a pivotal role in differentiation block. (**A** and **B**) 32Dcl3 cells transduced with pMYs-IP/pMYs-IB, pMYs-IP/ pMYs-ASXL1-MT2-IB, pMYs-Clec5a-IP/pMYs-ASXL1-MT2-IB, and pMYs-Clec5a-K16A-IP/pMYs-ASXL1-MT2-IB were cultured in the presence of 50 ng/ml G-CSF for 6 days. The proportions of mature or immature cells (**A**) and cytospin preparations of these cells (**B**) are shown. Images were obtained with a BX51 microscope and an Olympus DP12 camera with a UplanFl objective lens. Original magnification, ×40; scale bars: 20 μm. Data are representative of 3 independent experiments. (**C**) Relative expression levels of *CLEC5A* were examined by qRT-PCR in whole BM cells derived from normal controls and from patients with *ASXL1*-mutated MDS and *ASXL1*-WT MDS. The values were normalized by *GAPDH* mRNA levels. All data with error bars are presented as mean ± SEM of 2 independent experiments. *P* values were calculated using the 2-tailed Student's *t* test or the Cochran-Cox test.

pMXs-FLAG-ASXL1-MT2-IG (IRES-GFP), and the transduced cells were transplanted into sublethally irradiated Ly5.1 mice. In the transplanted mice, the percentage of the GFP-positive cells gradually increased in the peripheral blood and reached 41%–100% one year after transplantation, while it gradually decreased over time in the mice transplanted with ASXL1-WT– or empty vector–transduced BM cells (Figure 4A). GFP-positive cells in the BM of ASXL1-MT–transduced mice 6 months after the transplantation were mostly CD11b positive and included relatively few B220-positive cells, while GFP-negative, nontransduced cells consisted of equal numbers of CD11b-positive and B220-positive cells (Figure 4B). All of the transplanted mice displayed more or less morphological abnormalities 12 months or more after transplantation, mainly in myeloid cells and red blood cells (Figure 4C), including Pelger-Huet anomaly and hypersegmentation for myeloid cells and Howel-Jolly bodies, polychromasia, and anisopoikilocytosis for erythrocytes, consistent with multi-lineage dysplasia of human MDS. Mice expressing ASXL1-MT died of MDS after a long latency (median survival, 400.5 days), while most of the mock-transduced mice survived nearly 2 years without developing myeloid malignancies (Figure 4D). The GFP-positive BM cells that increased in ASXL1-MT–transduced mice were positive for CD11b and weakly positive for Gr1 and CD34. Expression of c-kit varied from positive to negative. These data suggest that a GFP-positive population contains immature and mature myeloid cells (Figure 4E). These mice developed severe anemia, leukopenia, and thrombocytopenia, while the BM was hypercellular and the spleen was enlarged (Figure 4, F and G). Thus, ASXL1-MT–transduced MDS mice developed pancytopenia with dysplasia in granulocytes and erythroid cells and occasionally progressed to overt leukemia, displaying all the features of human MDS. Overexpression of ASXL1-MT1 in the same BMT model revealed basically identical results (Supplemental Figure 4).

Expression profiles of hemopoietic cells of the mice that developed MDS. To elucidate the molecular mechanisms by which ASXL1-MT induced MDS, we performed expression profiles of BM cells of mice that developed MDS. We used $CD3^-B220^-Ter119^-$ BM cells of mock-transduced mice as a control. Gene set enrichment analysis (GSEA) indicated that ASXL1-MT induced an expression profile that inversely correlated with known PRC target genes (22), suggesting that ASXL1-MT inhibited PRC (Figure 5A). We also examined the expression of *Hoxa* genes and *Clec5a* in BM cells of the mice that developed MDS or MDS/AML after transplantation of ASXL1-MT–transduced BM cells; the expression of posterior *Hoxa* genes was increased and that of *Clec5a* was decreased in BM cells of MDS or MDS/AML mice when compared with BM cells of mock-transduced mice (Figure 5B). We next performed ChIP of the promoter regions of posterior *Hoxa* genes using H3K27me3 antibodies and found that H3K27me3 was greatly decreased around the promoter regions of *Hoxa5*, *Hoxa9*, and *Hoxa10* in the MDS mice, correlating well with the upregulation of their mRNA expression (Figure 5, B and C). In addition, Western blot analysis of purified histones in 32Dcl3 cells transduced with ASXL1-MT indicated that H3K27me3 was reduced globally (Figure 5D).

Interestingly, *HOXA9* expression was increased in whole BM cells of most MDS patients harboring *ASXL1* mutations, while the changes in *HOXA9* expression was not significant in MDS patients without *ASXL1* mutations (Figure 5E).

ASXL1-MT collaborated with N-Ras-G12V in inducing leukemia. ASXL1 knockdown reduces the latency and increases the severity

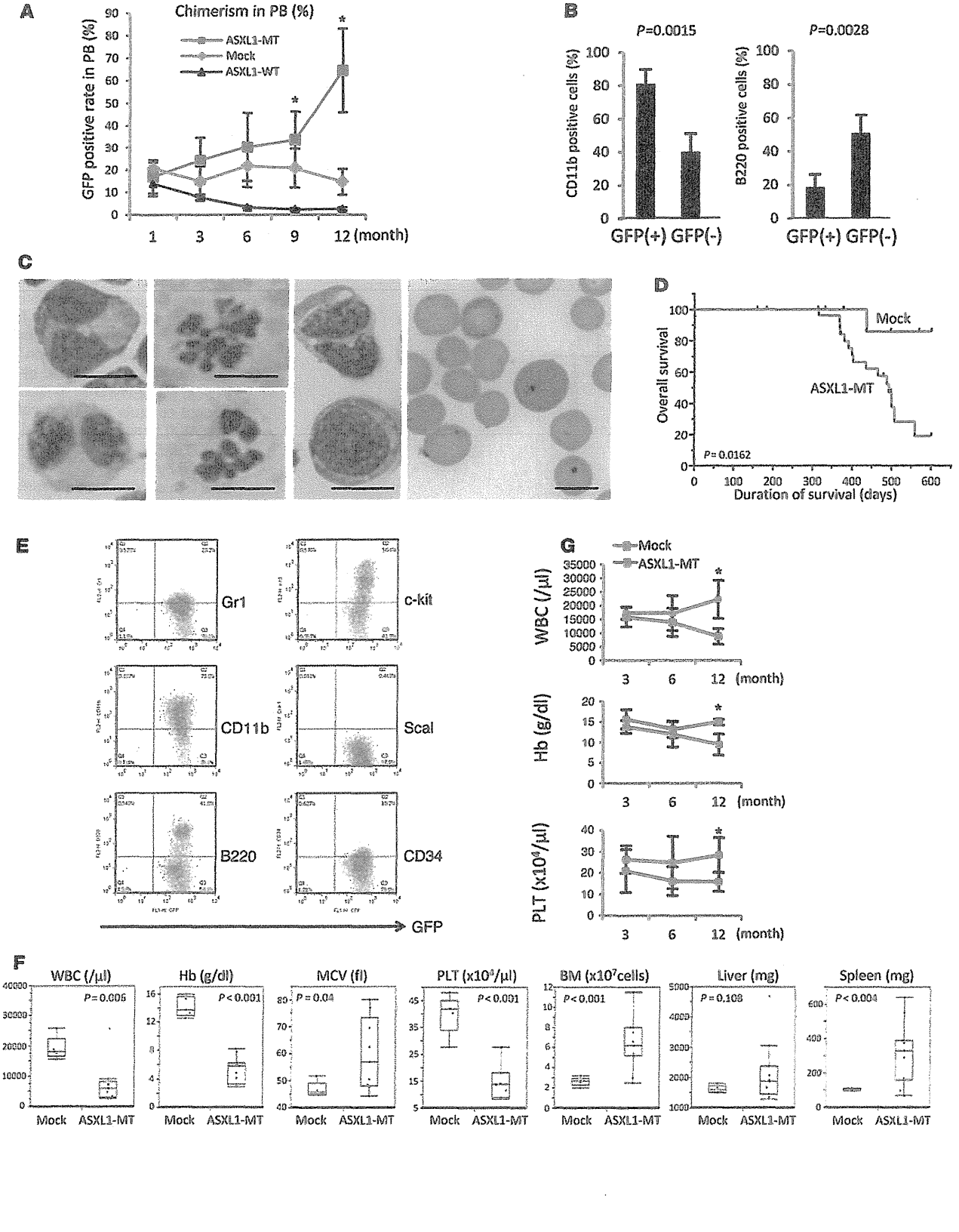

Figure 4
ASXL1 mutations induce MDS-like symptoms in a mouse BMT model. (**A**) Percentage of chimerism of donor cells in peripheral blood (PB). The chimerism of Ly5.1 donor–derived GFP-positive cells in PB (mean ± SEM) was examined after transplantation: mock, $n = 6$; ASXL1-MT, $n = 12$; ASXL1-WT, $n = 6$. (**B**) Percentages of CD11b-positive or B220-positive cells related to GFP positivity in the BM of the transplanted mice determined by flow cytometric analyses. Samples were obtained from mice with pMYs-FLAG-ASXL1-MT2-IG, sacrificed 6 months after transplantation ($n = 5$). (**C**) Dysplasias of hematopoietic cells in mice receiving transplants of ASXL1 mutants were observed. Scale bars: 10 μm. (**D**) Kaplan-Meier analysis for the survival of mice that received transplants of BM cells transduced with pMYs-IG (mock, $n = 13$, blue line) and pMYs-FLAG-ASXL1-MT2-IG (ASXL1-MT, $n = 25$, red line). *P* values were calculated using a log-rank test. (**E**) Flow cytometric analyses of BM cells derived from mice with ASXL1-MT. (**F**) Mice transplanted with ASXL1-MT2 (ASXL1-MT, $n = 11$) displayed progressive pancytopenia, macrocytosis, and hyperplastic BM and increased splenomegaly compared with mice transplanted with empty vector (mock, $n = 5$). BM cells were isolated from the femurs and tibias of the sacrificed mice. (**G**) Blood count data, including white blood cells (WBC), hemoglobin (Hb), and platelets (PLT), at 3, 6, or 12 months after transplantation are indicated (mean ± SEM). Mock, $n = 6$; ASXL1-MT, $n = 12$. $^*P < 0.05$.

of myeloproliferation induced by N-Ras-G12D (11). We thus examined whether stable expression of ASXL1-MT might similarly collaborate with N-Ras-G12V in vivo. As reported, N-Ras-G12V induced MPN-like diseases in the BMT model (23). In this model, co-transduction of ASXL1-MT, but not ASXL1-WT, with N-Ras-G12V significantly shortened latency when compared with mice transplanted with BM cells transduced with N-Ras-G12V alone (Figure 6A and data not shown) and increased the number of immature blast cells (35% vs. 15%), indicating that the combination of N-Ras-G12V and ASXL1-MT induced progression to AML rather than MPN (Figure 6, B and C). It also enhanced hepatosplenomegaly in the affected mice (Figure 6, D and E), while hemoglobin concentrations and number of white blood cells did not change significantly (Figure 6F). The expression of *Hoxa9* was increased in leukemic cells induced by ASXL1-MT and N-Ras-G12V when compared with that in MPN cells induced by N-Ras-G12V alone (Figure 6G), suggesting that ASXL1-MT inhibited PRC2-driven repression of transcription. On the other hand, expression of *Clec5a* was significantly decreased in leukemic cells induced by ASXL1-MT and N-Ras-G12V (Figure 6G). Other surface markers of MPN or AML cells induced by N-Ras-G12V or N-Ras-G12V and ASXL1-MT, respectively, were similar, although expression of CD11b and c-kit was slightly higher in N-Ras-G12V and ASXL1-MT–induced AML compared with N-Ras-G12V–induced MPN (Figure 6H). Thus, ASXL1-MT accelerated the onset of MPN induced by N-Ras-G12V and resulted in moderate increase in immature blasts and leukemic transformation, with increased expression of *Hoxa9* and decreased expression of *Clec5a*.

miR-125a is responsible for the repression of Clec5a by ASXL1-MT. As shown in Figure 5D, H3K27me3, a transcriptionally repressive mark, was globally reduced by ASXL1-MT. In order to ascertain whether a miRNA involved in myeloid transformation might be upregulated with ASXL1 mutations, we performed microarray analysis of miRNAs in ASXL1-MT–transduced BM cells and mock-transduced BM cells of the BMT model. We identified increased expression of several miRNAs in BM cells expressing ASXL1-MT, including miR-671, miR-125a, miR-714, miR-18b, miR-129, and miR-3107 (Supplemental Table 1). Among these, miR-125a is known to regulate hematopoietic stem cell numbers and induce MPN in a mouse BMT model (4, 24). A closely related miRNA, miR-125b, induces a variety of hematologic malignancies in transgenic mice and BMT models (25–27). We confirmed that expression of miR-125a was increased in 32Dcl3 cells expressing ASXL1-MT when compared with those expressing ASXL1-WT or the empty vector (Supplemental Figure 5). We next evaluated whether *Clec5a* is a target gene of miR125a. We identified a recognition site of miR-125a in the 3′ untranslated region (3′UTR) of mouse *Clec5a* and 2 recognition sites in the 3′UTR of human *CLEC5A* (Figure 7A). Therefore, we focused on Mus musculus miR-125a (*mmu-miR-125a*) and further investigated the effects of miR-125a expression.

First, to confirm that the 3′UTR of the murine *Clec5a* gene was targeted by miR-125a, we generated an EF1α promoter–driven luciferase construct harboring the 3′UTR of the *Clec5a* gene (Figure 7B) and performed a luciferase assay. As expected, the presence of the 3′UTR of the *Clec5a* gene reduced luciferase activity (Figure 7C). This reduction was completely cancelled by mutating the miR-125a target sequence in the 3′UTR of the *Clec5a* gene (Figure 7, B and C). miR-125b1 and miR-125b2 are genes distinct from miR-125a, but their seed sequence is identical with that of miR-125a. When miR-125a or miR-125b was expressed in 32Dcl3 cells, *Clec5a* expression was reduced both at mRNA levels and surface expression levels (Figure 7, D and E) compared with 32Dcl3 cells transduced with empty vector. Moreover, these cells became more resistant to G-CSF–induced differentiation (Figure 7F). These results clearly demonstrate that miR-125a targets *Clec5a* expression, leading to the inhibition of differentiation.

We next examined H3K27me3 near the transcription start site (TSS) of miR-125a in 32Dcl3 cells transduced with the empty vector, ASXL1-MT, or ASXL1-WT. This revealed profound reduction of H3K27me3 near the TSS of miR-125a in 32Dcl3 cells expressing ASXL1-MT (Figure 8, A–C). Moreover, H3K27me3 near the TSS of miR-125a was also reduced in BM cells of the mice that developed MDS after the transplantation of the ASXL1-MT–transduced BM cells, when compared with cells from mice engrafted with control BM cells (Figure 8, A, D, and E). Intriguingly, EZH2 binding to the miR-125a locus was reduced in ASXL1-MT–expressing 32Dcl3 cells or in ASXL1-MT–transduced BM cells from mice that developed MDS, while ASXL1-WT seemed to increase EZH2 binding to the miR-125a locus (Figure 8, B and D). Altogether, these results indicated a scenario in which ASXL1-MT hampered EZH2 binding to the miR-125a locus and suppressed EZH2-mediated H3K27me3 near the TSS of the miR-125a gene, leading to derepression of miR-125a. The increased miR-125a expression inhibited the expression of *Clec5a*, contributing to the impaired differentiation of mouse BM cells that developed MDS.

Discussion

We have established and characterized a mouse MDS model induced by *ASXL1* mutations. Although MDS patients frequently harbor multiple somatic mutations, it is not clear whether combinations of multiple mutations are required for the development of MDS. In addition, the molecular mechanisms of MDS pathogenesis remain elusive, particularly for recently identified mutations in epigenetic factors. Here we demonstrate that expression of the ASXL1-MT alone induces MDS in the mouse BMT model after a

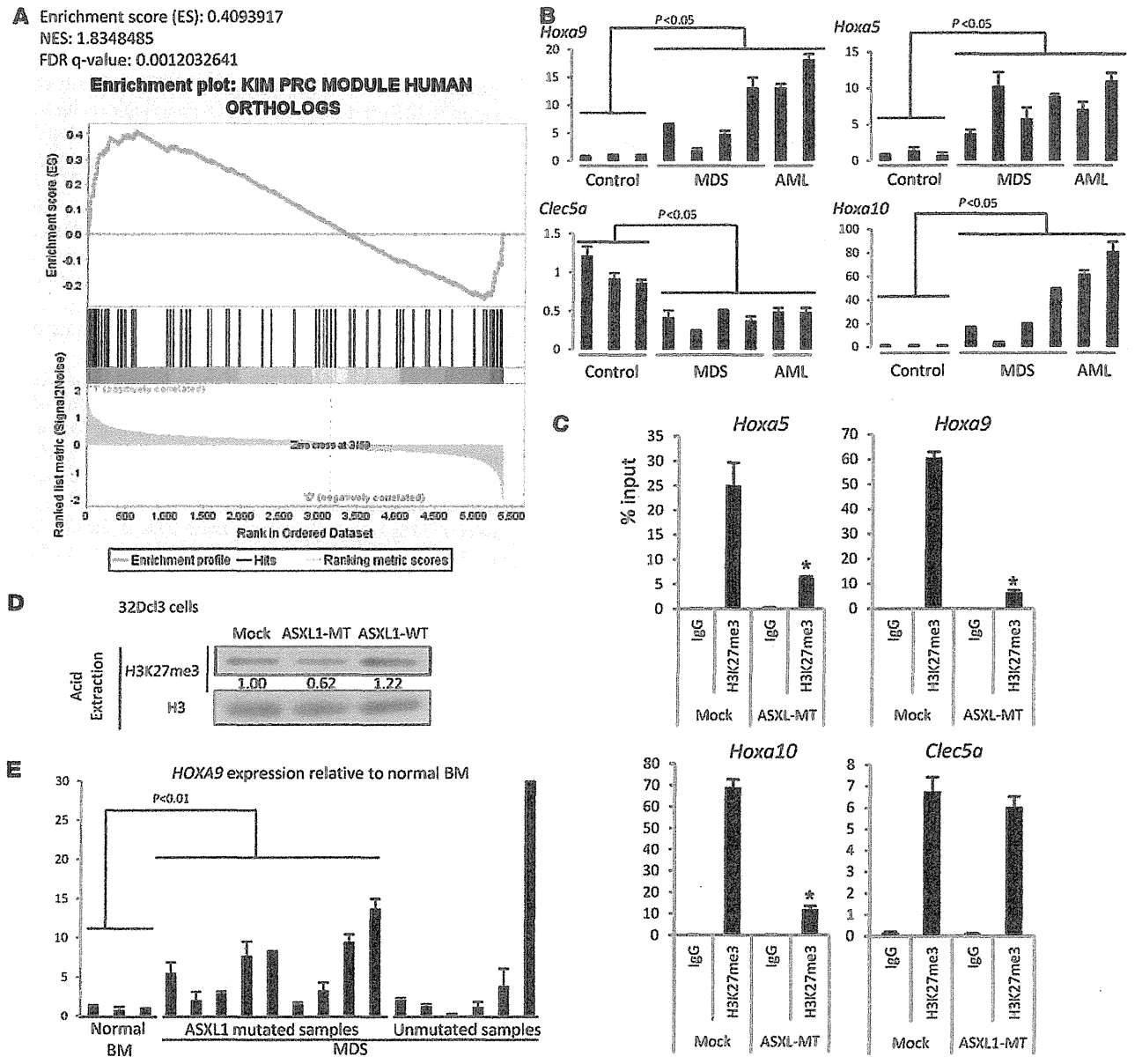

Figure 5

ASXL1-MT inhibited EZH2 functions, leading to loss of H3K27me3 at the *HoxA* locus. (**A**) GSEA of microarray analysis of mice with ASXL1-MT revealed a significant enrichment of genes found in a previously described gene expression signature of the PRC target, compared with that of mice with empty vectors. (**B**) In the mouse BMT model, ASXL1-MT–induced MDS/AML resulted in increased *Hoxa5*, *Hoxa9*, and *Hoxa10* and decreased *Clec5a* mRNA expression as shown by qRT-PCR analysis in BM cells from transplanted mice. (**C**) ChIP for H3K27me3 followed by qPCR across the *Hoxa5*, *Hoxa9*, *Hoxa10*, and *Clec5a* locus in BM cells of mice that received transplants of BM cells transduced with pMYs-IG (mock) or pMYs-FLAG-ASXL1-MT-IG (ASXL1-MT). (**D**) Acid-extracted histones were obtained from 32Dcl3 cells transduced with pMYs-IG, pMYs-FLAG-ASXL1-MT-IG, and pMYs-FLAG-ASXL1-WT-IG, and then analyzed by Western blotting using anti-H3K27me3 antibodies. Levels of histone modifications were normalized to the amount of histone H3 and are indicated using ImageJ. (**E**) Relative expression levels of *HOXA9* were examined by qRT-PCR in whole BM cells derived from normal controls and from patients with *ASXL1*-mutant MDS and *ASXL1*-WT MDS. The values were normalized by GAPDH mRNA levels.

long latency, indicating that ASXL1-MT is a driver mutation in MDS development. Mutations in *ASXL1* have been reported in patients with the entire spectrum of myeloid malignancies and are recurrently associated with adverse overall survival, independent of conventional clinical predictors (8, 28); this highlights a critical need to understand the precise mechanism of transformation by *ASXL1* mutations. Recently, it was indicated that a subset of *ASXL1* mutations result in loss of stable expression of full-length *ASXL1*

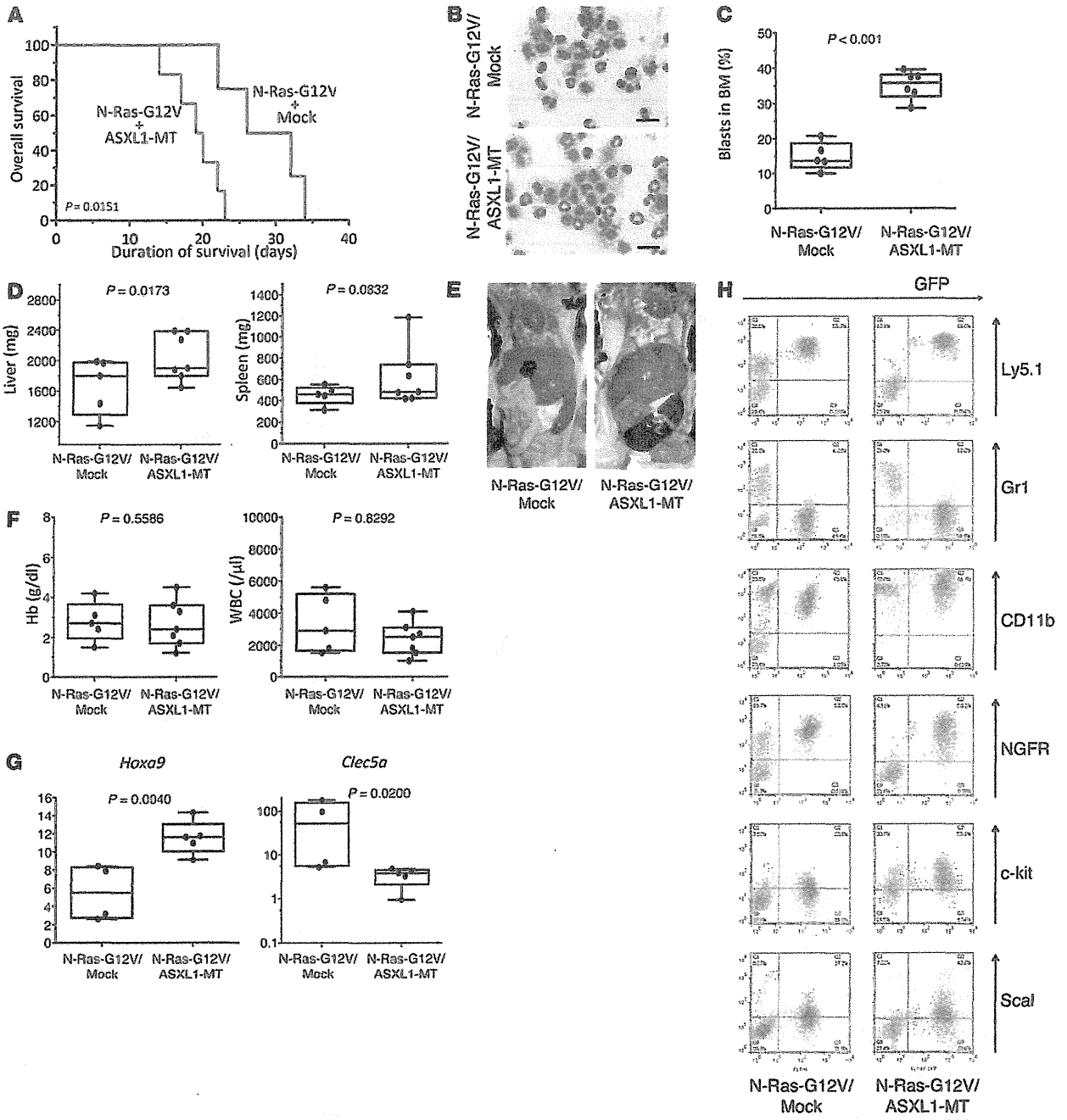

Figure 6

ASXL1 mutations collaborated with the N-Ras activating mutation in inducing myeloid leukemia. (**A**) Kaplan-Meier analysis for the survival of mice that received transplants of BM cells transduced with pMYs-N-Ras-G12V-IG and pMYs-INGFR (N-Ras-G12V + mock, $n = 4$, blue line) and pMYs-N-Ras-G12V-IG and pMYs-ASXL1-MT2-INGFR (N-Ras-G12V + ASXL1-MT, $n = 6$, red line). *P* values were calculated using a log-rank test. (**B**) Cytospin preparations of BM cells derived from mice transplanted with N-Ras-G12V + mock and N-Ras-G12V + ASXL1-MT were stained with Giemsa. Representative photographs are shown. Original magnification, ×400; scale bars: 20 μm. (**C** and **D**) Mice transplanted with N-Ras-G12V/ASXL1-MT displayed increased numbers of leukemic blasts in BM (**C**) and hepatomegaly and splenomegaly (**D**), although the differences in spleen weight were not statistically significant. *P* values were calculated using the Student's *t* test (**C**) or Cochran-Cox test (**D**). (**E**) Macroscopic findings of sacrificed mice transplanted with BM cells transduced with the indicated construct. Representative photographs are shown. (**F**) Mice transplanted with N-Ras-G12V/mock and N-Ras-G12V/ASXL1-MT displayed severe anemia and leukopenia to a similar extent. (**G**) qRT-PCR revealed an increased expression of *Hoxa9* and decreased expression of *Clec5a* in the BM of mice transplanted with N-Ras-G12V/ASXL1-MT. *P* values were calculated using the Cochran-Cox test. (**H**) Flow cytometric analysis of BM cells derived from sacrificed mice transduced with indicated constructs.

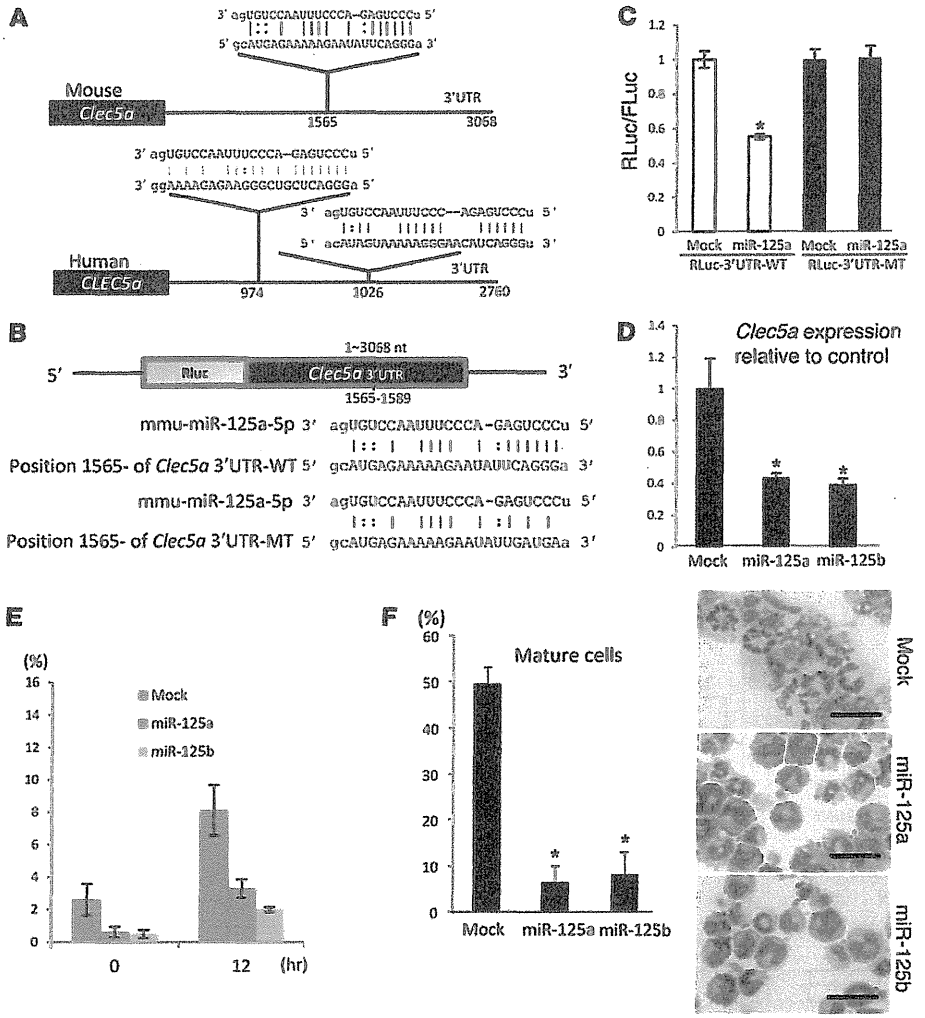

Figure 7

ASXL1 mutations caused upregulation of miR-125a, leading to the repression of *Clec5a*. (**A**) Schematic presentation of predicted miR-125a–binding sites in the mouse *Clec5a* (top) and human *CLEC5A* 3′UTR (bottom). (**B**) To confirm that *Clec5a* is a direct target gene of miR-125a, the WT 3′UTR of *Clec5a* or the mutated 3′UTR was cloned to downstream of the Renilla luciferase (Rluc) open reading frame. Schematic diagrams of predicted miR-125a–binding sites in the *Clec5a*-3′UTR and the alignment between miR-125a and either *Clec5a*-3′UTR (top) or a mutated 3′UTR (bottom) are shown. Three bases in the 3′UTR, corresponding to seed sequences, were replaced with the indicated bases in the mutant form. (**C**) 293T cells were cotransfected with an internal control vector (pGL3-control) plus either pGL4.74[hRluc/TK]-Clec5a3′UTR-WT or pGL4.74[hRluc/TK]-Clec5a3′UTR-MT plus either pMXs-EF1-miR-125a-Puro or mock (pMXs-EF1-Puro). Luciferase assays were performed with a triplicate set. (**D**) Relative expression levels of *Clec5a* by qRT-PCR in 32Dcl3 cells transduced with pMXs-EF1-Puro (mock), pMXs-EF1-miR-125a-Puro, and pMXs-EF1-miR-125b-Puro. (**E**) Positive rate of Clec5a expression in 32Dcl3 cells transduced with mock, miR-125a, or miR-125b after incubation with 1 ng IL-3 (0 hours) or 50 ng/ml G-CSF (12 hours) was analyzed by flow cytometry at indicated time points. (**F**) The proportion of mature cells (left) and cytospin preparations (right) of the 32Dcl3 cells expressing mock, miR-125a, or miR-125b cultured in the presence of 50 ng/ml G-CSF for 6 days. Scale bars: 20 μm. $^*P < 0.05$.

and that depletion of ASXL1 promoted myeloid transformation through impaired PRC2-mediated H3K27 methylation (11).

ASXL1 mutations mostly occur as heterozygous mutations, and the mutations conspicuously occur as nonsense and frameshift mutations in the last exon, prior to the PHD domain. This suggests that most *ASXL1* mutations result in a stable protein product that may have gain-of-function mutations. Here we identify that stable expression of ASXL1-MT, which results in global downregulation of H3K27me3, impaired myeloid differentiation and collaborated with co-occurring genetic alterations, as was seen with downregulation of ASXL1-WT. The observation that expression of ASXL1-MT mirrors the effects of downregulation of ASXL1-WT strongly suggests that in addition to known loss-of-function mutations, a subset of *ASXL1* mutations confer dominant-negative activity.

Expression of ASXL1-MT as demonstrated here resulted in impaired myeloid differentiation in vitro and in vivo. *ASXL1*

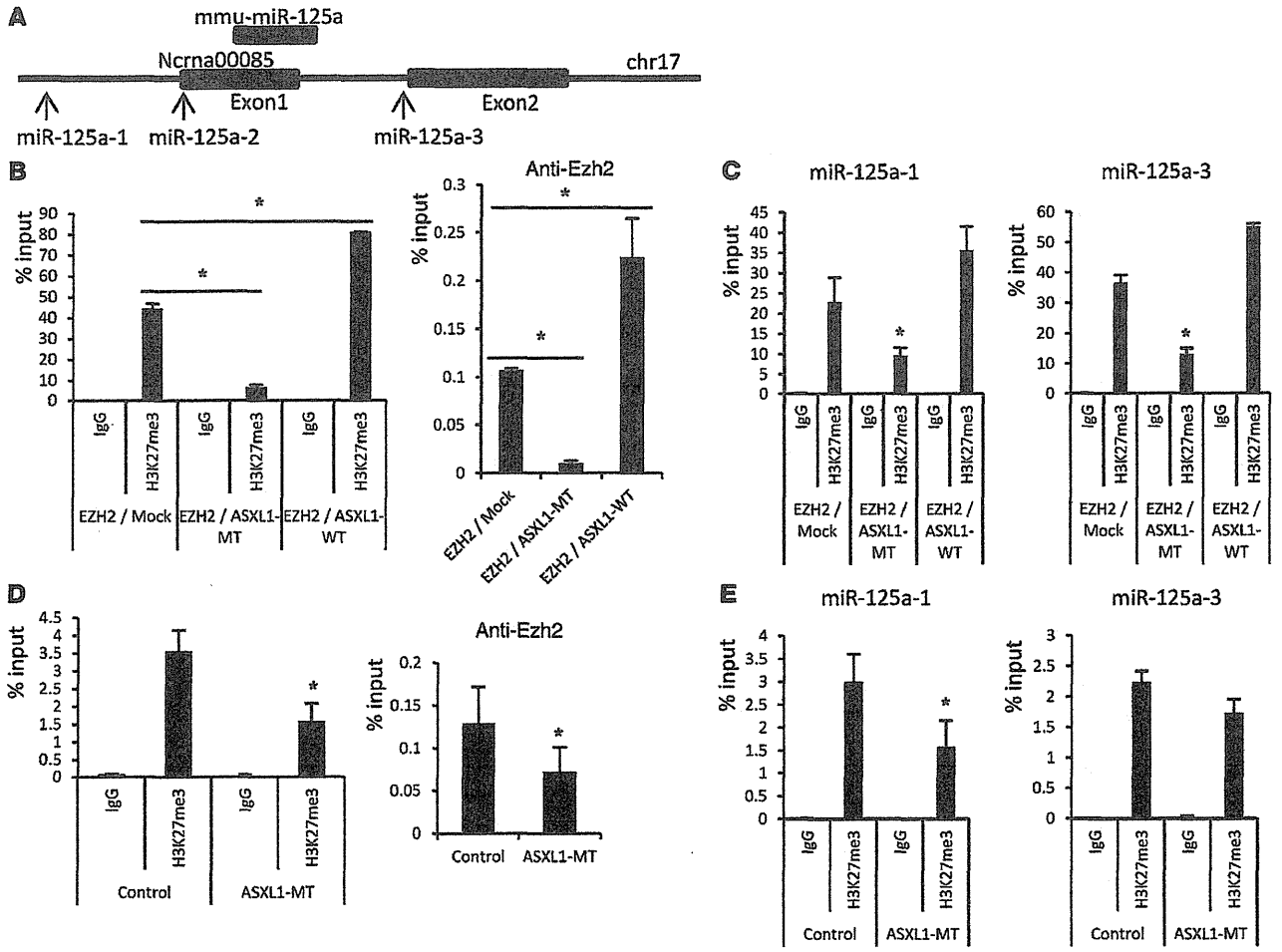

Figure 8

ASXL1 mutations caused loss of H3K27me3 at the miR-125a locus. (**A**) Schematic diagram of the mmu–miR-125a and Ncrna00085 loci indicating their genomic structures. Exons are indicated by black boxes. Regions amplified from the precipitated DNA by site-specific quantitative PCR are indicated by arrows. (**B**–**E**) Quantitative ChIP analyses of 32Dcl3 cells transduced with pMYs-EZH2-IG and pMYs-IP (EZH2/mock), pMYs-EZH2-IG and pMYs-FLAG-ASXL1-MT2-IP (EZH2/ASXL1-MT), or pMYs-EZH2-IG and pMYs-FLAG-ASXL1-WT-IP (EZH2/ASXL1-WT) (**B** and **C**) and BM cells from the mice transplanted with BM cells transduced with pMYs-IG (Mock) or pMYs-FLAG-ASXL1-MT2 (ASXL1-MT) (**D** and **E**). Abs specific to H3K27me3 or Ezh2 and primers for miR-125a-2 (**B** and **D**) and for miR-125a-1/3 (**C** and **E**) were used for ChIP analyses. There were no detectable or very low levels of background signals with IgG isotype controls at all amplified regions. Percentages of input DNA are shown as the mean ± SEM for duplicate analyses. $^*P < 0.05$. Data are representative of 3 independent experiments.

mutations are most frequent in patients with MDS, MDS/MPN overlap syndromes, and AML with myelodysplasia-related changes, highlighting a close relationship between impaired myeloid differentiation and *ASXL1* mutations (29). We identified that expression of ASXL1-MT in vivo results in the development of a lethal disorder characterized by morphologic dysplasia, leukopenia, and impaired myeloid differentiation with subsequent transformation to AML in some cases, all hallmarks of human MDS. Moreover, co-expression of mutant forms of ASXL1 with oncogenic N-RAS, a complex genotype common to patients with CMML (10), results in a lethal myeloid malignancy with shorter latency than that seen with oncogenic N-RAS alone. Given the paucity of genetically accurate murine models of MDS, expression of ASXL1-MT as demonstrated here may be quite valuable for further mechanistic and preclinical studies of MDS and AML with myelodysplasia-related changes. Interestingly, it has been recently reported that disruption of the ASXL1-interacting molecule BAP1 in mice induced CMML-like disease (30). *BAP1* mutation was also identified in a patient with MDS, implicating the BAP1-ASXL1 axis in suppressing MDS. The contribution of disruption of the ASXL1-BAP1 axis (PRC1 related), versus loss of H3K27 trimethylation (PRC2 related), in promoting myeloid transformation induced by ASXL1-MT requires further evaluation.

To understand the transcriptional events responsible for the biological effects of *ASXL1* mutations in more detail, we performed transcriptomic studies in the presence of mutant ASXL1 in vitro and in vivo. In addition to identifying significant upregulation of posterior *Hoxa* genes, we identified increased expression of miR-125a due to locus-specific downregulation of H3K27 methylation. Moreover, it has been reported that miR-125a is upregulated after inhibition of *EZH2* by knockdown

in DU145 prostate cancer cells (31). miR-125a was the only miR upregulated in both our murine system and in primary human MDS samples (32). miR-125a belongs to the miRNA family that also includes miR-125b1 and miR-125b2, all of which have the same seed sequence and have been implicated in human leukemia/lymphoma (33–35) as well as in MDS (32). Forced expression of these miRs has been previously shown to induce the expansion of hemopoietic stem cells or hamper myeloid differentiation (4, 24-26, 32, 35).

Although several proapoptotic genes have been implicated for hematopoietic transformation as miR-125a targets (4, 26, 36), here we identified direct repression of a novel target *Clec5a* by miR-125a as a specific effector of the differentiation phenotype. The type II membrane protein CLEC5A (20) belongs to the lectin family and associates with the adaptor protein DAP12 to transmit positive signals. It was previously recognized that *Clec5a* expression is correlated with myeloid differentiation, as *Clec5a* is expressed in monocytes and neutrophils, and its expression is increased by granulocytic differentiation of 32Dcl3 cells (21) and monocytic differentiation of U937 cells and primary progenitor cells (37). Here we present clear evidence that *Clec5a* supports myeloid differentiation. First, ASXL1-MT but not ASXL1-WT reduced expression of *Clec5a* in 32Dcl3 cells and impaired G-CSF–induced granulocytic differentiation. Second, in 32D3 cells expressing ASXL1-MT, myeloid differentiation was partly restored by the forced expression of Clec5a, but not by a mutant Clec5a (Clec5a-K16A) that cannot associate with DAP12. Third, knockdown of *Clec5a* impaired G-CSF–induced differentiation of 32Dcl3 cells. In addition, *Clec5a* expression was downregulated in the ASXL1-MT–induced MDS mice. These results indicate that downregulation of *Clec5a* by ASXL1-MT impairs myeloid differentiation and is involved in MDS development. Interestingly, while *HOXA9* expression was high in MDS patients with *ASXL1* mutations (Figure 5E), the expression level of *CLEC5A* was generally low in MDS patients compared with controls and did not correlate with the presence of *ASXL1* mutations (Figure 3C). This suggests that *CLEC5A* expression is reduced in MDS by multiple causes including *ASXL1* mutations, and that reduction of *CLEC5A* might play a general role in the pathogenesis of MDS. Prior data indicating downregulation of *CLEC5A* expression in acute leukemia likewise support the possibility that *CLEC5A* downregulation may be important in the pathogenesis of multiple subtypes of myeloid malignancies (38).

The data presented here indicate that *ASXL1* mutations, which result in a truncated protein product, may (a) inhibit PRC2 function in a dominant-negative fashion and (b) promote myeloid transformation through impaired PRC2-mediated repression of posterior *HOXA*s and miR-125a and subsequent miR-125a suppression of *CLEC5A*. Thus, although changes in expression of other genes caused by *ASXL1* mutations may also be involved, it is documented that the derepression of *HOXA*s and miR-125a and the suppression of *CLEC5A* contribute to the development of MDS. Given the clinical importance of *ASXL1* mutations, the identification of gain-of-function *ASXL1* mutations is critical, as it provides a rationale for therapies aimed at targeting the expressed mutant forms of ASXL1. Finally, the data here provide further basis for the involvement of miR-125 in myeloid malignancy pathogenesis and identify an important role for *CLEC5A* in the pathogenesis of multiple genetic subtypes of myeloid malignancies.

Methods

Mice. C57BL/6 (Ly5.1) mice (Sankyo Labo Service Corporation) and C57BL/6 (Ly5.2) mice (Charles River Laboratories Japan) were used for BMT experiments.

Cell culture. HEK293T cells were cultured in DMEM supplemented with 10% FBS. Human leukemia cell lines were cultured in RPMI-1640 supplemented with 10% FBS (HL60, U937, K562, KU812, TS9;22, and MEG-01 cells), RPMI-1640 supplemented with 20% FBS (SET2, NOMO1, and Mono-Mac-6 cells), RPMI-1640 medium supplemented with 10% FBS/1 μM hydrocortisone/10% horse serum (UKE1 cells) or IMDM with 20% FBS (KBM5 cells). The murine myeloid cell lines 32Dcl3 and FDC-P1 were grown in RPMI-1640 medium supplemented with 10% FBS, antibiotics, L-glutamine, and 1 ng/ml IL-3. Before the assays for proliferation and differentiation, the transduced 32Dcl3, HL60, or FDC-P1 cells were GFP sorted or subjected to drug selection with 1 μg/ml puromycin and/or 10 μg/ml blasticidin, if necessary.

Vector construction. We used the retrovirus vectors pMYs-FLAG-ASXL1-WT-IG and pMYs-FLAG-ASXL1-MT-IG, in which ASXL1-WT or ASXL1-MT (1934dupG;G646WfsX12 or 1900–1922del;E635RfsX15, respectively), tagged with a FLAG epitope at the N terminus, was inserted upstream of the IRES-EGFP cassette of pMYs-IG (39). Similarly, WT Clec5a or Clec5a-K16A was inserted upstream of the IRES-puro to generate pMYs-Clec5a-IP or pMYs-Clec5a-K16A-IP. ASXL1-MT was subcloned upstream of the IRES-blasticidin cassette of pMYs-IB. Likewise, Myc-tagged EZH2 was subcloned into pMYs-IG to generate pMYs-Myc–tagged EZH2-IG. To perform the mouse BMT model, we constructed pMYs-N-Ras-G12V-IG and pMYs-ASXL1-MT-IRES–nerve growth factor receptor (pMYs-ASXL1-MT-IRES-NGFR). For knockdown assays, shRNA expression fragments were cloned into pMXs-U6-GFP or pMXs-U6-Puro, which were pMXs-based, self-inactivating retrovirus vectors expressing shRNA under a U6 promoter with a PGK promoter–driven GFP or puromycin-resistant gene expression. An shRNA expression cassette was constructed in the opposite direction from a GFP/Puro expression cassette. We also constructed microRNA vectors as described previously (26). Briefly, miRNA expression fragments were cloned into pMXs-EF1-Puro vector.

Transfection and retrovirus production. Retroviral production was done as described previously (40). Briefly, retroviruses were generated by transient transfection of Plat-E packaging cells with using the calcium-phosphate coprecipitation method. Cell lines such as 32Dcl3 were infected with the retroviruses as previously described (39).

Mutation analysis of ASXL1. Somatic mutations of *ASXL1* genes were searched by sequencing exons after PCR amplification of genomic DNA, as described previously (6).

qRT-PCR. Total RNAs were treated with deoxyribonuclease I (Invitrogen) and reverse transcribed by using High Capacity cDNA Reverse Transcription Kits (Applied Biosystems) or miScript Reverse Transcription Kit (QIAGEN). qRT-PCR was performed using a Rotor-Gene Q (QIAGEN). For mRNA RT-PCR, a SYBR Premix EX Taq (Takara) was used as previously described (41). Mature miR-125a expression was measured using a miScript SYBR Green PCR kit (QIAGEN). cDNA was amplified with miR-125a–specific primers (QIAGEN). Expression of RNA, U6 small nuclear 2 (RNU6B) as an internal control was used for normalization of the results. All data with error bars indicate the mean ± SEM.

Mouse BMT. Mouse BMT was performed as described previously (40). Briefly, BM mononuclear cells were isolated from the femurs and tibias of C57BL/6 (Ly-5.1) donor mice 3 days after intraperitoneal administration of 150 mg/kg 5-fluorouracil. The cells were stimulated with 50 ng/ml of mouse stem cell factor, mouse FLT3 ligand, mouse IL-6, and human thrombopoietin (all cytokines were from R&D Systems). The prestimulated cells were infected for 60 hours with the retroviruses harboring

pMYs-IG, pMYs-FLAG-ASXL1-MT-IG, pMYs-FLAG-ASXL1-WT-IG, pMYs-N-Ras-G12V-IG and pMYs-INGFR, or pMYs-N-Ras-G12V-IG and pMYs-ASXL1-MT-IRES-NGFR, using 6-well dishes coated with RetroNectin (Takara Bio). Then, 2×10^6 infected BM cells were injected into sublethally γ-irradiated C57BL/6 (Ly-5.2) recipient mice. Overall survival of transplanted mice was estimated using the Kaplan-Meier method. All animal studies were approved by the Animal Care Committee of the Institute of Medical Science at the University of Tokyo.

Flow cytometric analysis. Briefly, cells were stained with indicated phycoerythrin-conjugated antibodies (eBioscience). Flow cytometric analysis of the stained cells was performed with FACSCalibur Flow (BD Biosciences) equipped with FlowJo Version 7.2.4 software (TreeStar). All data with error bars indicate the mean ± SEM.

Analysis of cell growth. Cell growth was estimated by CellTiter-Glo Luminescent Cell Viability Assay (Promega). All data with error bars indicate the mean ± SEM.

Immunostaining. Immunostaining of 293T cells transiently transfected with retrovirus constructs was performed as described previously (42). After fixation with 1.5% paraformaldehyde, cells were immunostained with rabbit anti-Flag Ab. The cells were then stained with Alexa Fluor 546–conjugated goat anti-rabbit immunoglobulin G secondary Ab (Molecular Probes). Nuclei were counterstained with DAPI (4′,6-diamidino-2-phenylindole dihydrochloride). Fluorescent images were analyzed on a confocal microscope (FLUOVIEW FV300 scanning laser biological microscope JX70 system; Olympus) equipped with a SenSys/0L cold charge-coupled device camera (Olympus). An LCPlanFI ×60/1.40 NA oil was used as the objective lens. Data are representative of 3 independent experiments.

Western blot analysis. Cell lysates were subject to immunoblotting using the following antibodies: ASXL1 (clone 2049C2a; Santa Cruz Biotechnology catalog no. sc-81053; C-terminus directed), EZH2 (clone AC22; Cell Signaling Technologies catalog no. 3147), FLAG (M2 FLAG; Sigma-Aldrich catalog no. A2220), c-myc (clone 9E10; Roche catalog no. 11 667 203 001), H3K27me3 (CMA323) (43), total histone H3 (44), and tubulin (clone B-5-1-2; Santa Cruz Biotechnology catalog no. sc-23948). Antibodies different from the above used for immunoprecipitation include anti-EZH2 antibodies (Active Motif catalog no. 39901). Immunoprecipitation was performed in an immunoprecipitation buffer (150 mM NaCl, 50 mM Tris pH 7.5, 1 mM EDTA, 1% Triton, 2 mM sodium orthovanadate, 2 mM PMSF, 50 mM sodium fluoride). Western blot analysis of purified histone was performed as described previously (45). Data are representative of 3 independent experiments.

ChIP assay. ChIP assays were performed as described previously (43), except for the process of cross-link and quenching reactive aldehydes. In brief, 32cl3 cells or sorted BM cells ($2–5 \times 10^6$) were cross-linked with 1% formaldehyde for 5 minutes at room temperature and then incubated with 350 mM glycine for 5 minutes for quenching. These assays were carried out using the following antibodies: EZH2 (Active motif catalog no. 39901), H3K4me3 (CMA304), H3K9me3 (CMA318), H3K27me3 (CMA323) (43), and ubiquityl-histone H2AK119 (clone D27C4; Cell Signaling Technologies catalog no. 8240). Quantitative PCR was performed with a Rotor-Gene Q (QIAGEN) using SYBR Premix EX Taq (Takara). All data with error bars indicate the mean ± SEM. Data are representative of 3 independent experiments.

Differentiation assay. The 32Dcl3 cells were induced to differentiate to granulocytes by removing IL-3, washing them twice in RPMI medium without IL-3, and adding G-CSF (R & D Systems) to a final concentration of 50 ng/ml. Cells were cytocentrifuged (Cytospin4; Thermo Shandon), and cell morphologies were evaluated by Giemsa staining 3 or 6 days after G-CSF addition (46). FDC-P1 cells were washed in RPMI medium and then incubated in murine GM-CSF (10 ng/ml) for 6 days (47). HL60 cells were incubated in the medium supplemented with 10^{-6} M ATRA for 3 days. Images were obtained with a BX51 microscope and a DP12 camera (Olympus) with an Olympus UplanFl objective lens. All data with error bars indicate the mean ± SEM. Data are representative of 3 independent experiments.

Luciferase assay. Luciferase assays to investigate whether miRNA binds to the expected target sequence were performed as described previously (26). All data with error bars indicate the mean ± SEM.

Microarray data. Microarray data have been deposited in Gene Expression Omnibus (accession no. GSE49117 and GSE49118; http://www.ncbi.nlm.nih.gov/geo/).

Statistics. Statistical significance was calculated using the indicated tests for independent variables. All calculations were carried out using the program JMP 8.0 (SAS Institute Inc.). *P* values of less than 0.05 were considered significant using the 2-tailed Student's *t* test, unless otherwise noted. In box and whisker plots, the bottom and top of the box indicate the first and third quartiles, and the band inside the box is the second quartile (the median). The lowest or highest datum shows the minimum or maximum of all of data within 1.5 interquartile range of the lower or upper quartile.

Study approval. All animal studies were approved by the Animal Care Committee of the Institute of Medical Science at the University of Tokyo. MDS patients were diagnosed at Hannover Medical School. Diagnosis was based on the World Health Organization classification. Informed consent was obtained in accordance with the Declaration of Helsinki, and the studies were approved by the institutional review board of Hannover Medical School (ethical vote no. 5558) and by the ethics committees of the University of Tokyo (approval 20-10).

Acknowledgments

We thank Atsushi Iwama (Chiba University) and Makoto Nakanishi (Nagoya City University) for their helpful discussions and Shogo Yamamoto (The University of Tokyo) for microarray analysis. This work was supported by Grants-in-Aid for Scientific Research on Innovative Areas from the Ministry of Education, Culture, Sports, Science and Technology of Japan, and in part by a Grant-in-Aid for the Third-Term Comprehensive 10-Year Strategy for Cancer Control. We are grateful to Dovie Wylie for excellent language support.

Received for publication April 29, 2013, and accepted in revised form August 8, 2013.

Address correspondence to: Toshio Kitamura, Institute of Medical Science, University of Tokyo, 4-6-1 Shirokanedai, Minato-ku, Tokyo 108-8639, Japan. Phone: 81.3.5449.5759; Fax: 81.3.5449.5428; E-mail: kitamura@ims.u-tokyo.ac.jp.

1. Fisher CL, et al. Additional sex combs-like 1 belongs to the enhancer of trithorax and polycomb group and genetically interacts with Cbx2 in mice. *Dev Biol.* 2010;337(1):9–15.
2. Park UH, Yoon SK, Park T, Kim EJ, Um SJ. Additional sex comb-like (ASXL) proteins 1 and 2 play opposite roles in adipogenesis via reciprocal regulation of peroxisome proliferator-activated receptor {gamma}. *J Biol Chem.* 2011;286(2):1354–1363.
3. Cho YS, Kim EJ, Park UH, Sin HS, Um SJ. Additional sex comb-like 1 (ASXL1), in cooperation with SRC-1, acts as a ligand-dependent coactivator for retinoic acid receptor. *J Biol Chem.* 2006; 281(26):17588–17598.
4. Guo S, et al. Complex oncogene dependence in microRNA-125a-induced myeloproliferative neoplasms. *Proc Natl Acad Sci U S A.* 2012; 109(41):16636–16641.
5. Rocquain J, et al. Combined mutations of ASXL1, CBL, FLT3, IDH1, IDH2, JAK2, KRAS, NPM1, NRAS, RUNX1, TET2, and WT1 genes in myelodysplastic syndromes and acute myeloid leukemias. *BMC Cancer.* 2010;10:401.
6. Gelsi-Boyer V, et al. Mutations of polycomb-associ-

ated gene ASXL1 in myelodysplastic syndromes and chronic myelomonocytic leukaemia. *Br J Haematol.* 2009;145(6):788–800.
7. Boultwood J, et al. Frequent mutation of the polycomb-associated gene ASXL1 in the myelodysplastic syndromes and in acute myeloid leukemia. *Leukemia.* 2010;24(5):1062–1065.
8. Thol F, et al. Prognostic significance of ASXL1 mutations in patients with myelodysplastic syndromes. *J Clin Oncol.* 2011;29(18):2499–2506.
9. Gelsi-Boyer V, et al. ASXL1 mutation is associated with poor prognosis and acute transformation in chronic myelomonocytic leukaemia. *Br J Haematol.* 2010;151(4):365–375.
10. Abdel-Wahab O, et al. Concomitant analysis of EZH2 and ASXL1 mutations in myelofibrosis, chronic myelomonocytic leukemia and blast-phase myeloproliferative neoplasms. *Leukemia.* 2011; 25(7):1200–1202.
11. Abdel-Wahab O, et al. ASXL1 mutations promote myeloid transformation through loss of PRC2-mediated gene repression. *Cancer Cell.* 2012; 22(2):180–193.
12. Scheuermann JC, et al. Histone H2A deubiquitinase activity of the Polycomb repressive complex PR-DUB. *Nature.* 2010;465(7295):243–247.
13. Chung YR, Schatoff E, Abdel-Wahab O. Epigenetic alterations in hematopoietic malignancies. *Int J Hematol.* 2012;96(4):413–427.
14. Nikoloski G, van der Reijden BA, Jansen JH. Mutations in epigenetic regulators in myelodysplastic syndromes. *Int J Hematol.* 2012;95(1):8–16.
15. Vainchenker W, Delhommeau F, Constantinescu SN, Bernard OA. New mutations and pathogenesis of myeloproliferative neoplasms. *Blood.* 2011; 118(7):1723–1735.
16. Abdel-Wahab O, Kilpivaara O, Patel J, Busque L, Levine RL. The most commonly reported variant in ASXL1 (c.1934dupG;p.Gly646TrpfsX12) is not a somatic alteration. *Leukemia.* 2010;24(9):1656–1657.
17. Schnittger S, et al. ASXL1 exon 12 mutations are frequent in AML with intermediate risk karyotype and are independently associated with an adverse outcome. *Leukemia.* 2013;27(1):82–91.
18. Schlegelberger B, Gohring G, Thol F, Heuser M. Update on cytogenetic and molecular changes in myelodysplastic syndromes. *Leuk Lymphoma.* 2012; 53(4):525–536.
19. Gelsi-Boyer V, Brecqueville M, Devillier R, Murati A, Mozziconacci MJ, Birnbaum D. Mutations in ASXL1 are associated with poor prognosis across the spectrum of malignant myeloid diseases. *J Hematol Oncol.* 2012;5:12.
20. Bakker AB, Baker E, Sutherland GR, Phillips JH, Lanier LL. Myeloid DAP12-associating lectin (MDL)-1 is a cell surface receptor involved in the activation of myeloid cells. *Proc Natl Acad Sci U S A.* 1999; 96(17):9792–9796.
21. Aoki N, et al. Expression and functional role of MDL-1 (CLEC5A) in mouse myeloid lineage cells. *J Leukoc Biol.* 2009;85(3):508–517.
22. Kim J, et al. A Myc network accounts for similarities between embryonic stem and cancer cell transcription programs. *Cell.* 2010;143(2):313–324.
23. MacKenzie KL, Dolnikov A, Millington M, Shounan Y, Symonds G. Mutant N-ras induces myeloproliferative disorders and apoptosis in bone marrow repopulated mice. *Blood.* 1999;93(6):2043–2056.
24. Gerrits A, et al. Genetic screen identifies microRNA cluster 99b/let-7e/125a as a regulator of primitive hematopoietic cells. *Blood.* 2012;119(2):377–387.
25. Chaudhuri AA, et al. Oncomir miR-125b regulates hematopoiesis by targeting the gene Lin28A. *Proc Natl Acad Sci U S A.* 2012;109(11):4233–4238.
26. Enomoto Y, et al. Emu/miR-125b transgenic mice develop lethal B-cell malignancies. *Leukemia.* 2011; 25(12):1849–1856.
27. Bousquet M, Harris MH, Zhou B, Lodish HF. MicroRNA miR-125b causes leukemia. *Proc Natl Acad Sci U S A.* 2010;107(50):21558–21563.
28. Abdel-Wahab O, Patel J, Levine RL. Clinical implications of novel mutations in epigenetic modifiers in AML. *Hematol Oncol Clin North Am.* 2011; 25(6):1119–1133.
29. Devillier R, et al. Acute myeloid leukemia with myelodysplasia-related changes are characterized by a specific molecular pattern with high frequency of ASXL1 mutations. *Am J Hematol.* 2012;87(7):659–662.
30. Dey A, et al. Loss of the tumor suppressor BAP1 causes myeloid transformation. *Science.* 2012; 337(6101):1541–1546.
31. Cao Q, et al. Coordinated regulation of polycomb group complexes through microRNAs in cancer. *Cancer Cell.* 2011;20(2):187–199.
32. Rhyasen GW, Starczynowski DT. Deregulation of microRNAs in myelodysplastic syndrome. *Leukemia.* 2012;26(1):13–22.
33. Tassano E, Acquila M, Tavella E, Micalizzi C, Panarello C, Morerio C. MicroRNA-125b-1 and BLID upregulation resulting from a novel IGH translocation in childhood B-Cell precursor acute lymphoblastic leukemia. *Genes Chromosomes Cancer.* 2010;49(8):682–687.
34. Chapiro E, et al. A new recurrent translocation t(11;14)(q24;q32) involving IGH@ and miR-125b-1 in B-cell progenitor acute lymphoblastic leukemia. *Leukemia.* 2010;24(7):1362–1364.
35. Bousquet M, et al. Myeloid cell differentiation arrest by miR-125b-1 in myelodysplastic syndrome and acute myeloid leukemia with the t(2;11)(p21;q23) translocation. *J Exp Med.* 2008; 205(11):2499–2506.
36. Ooi AG, Sahoo D, Adorno M, Wang Y, Weissman IL, Park CY. MicroRNA-125b expands hematopoietic stem cells and enriches for the lymphoid-balanced and lymphoid-biased subsets. *Proc Natl Acad Sci U S A.* 2010;107(50):21505–21510.
37. Gingras MC, Lapillonne H, Margolin JF. TREM-1, MDL-1, and DAP12 expression is associated with a mature stage of myeloid development. *Mol Immunol.* 2002;38(11):817–824.
38. Batliner J, et al. CLEC5A (MDL-1) is a novel PU.1 transcriptional target during myeloid differentiation. *Mol Immunol.* 2011;48(4):714–719.
39. Kitamura T, et al. Retrovirus-mediated gene transfer and expression cloning: powerful tools in functional genomics. *Exp Hematol.* 2003;31(11):1007–1014.
40. Watanabe-Okochi N, et al. AML1 mutations induced MDS and MDS/AML in a mouse BMT model. *Blood.* 2008;111(8):4297–4308.
41. Enomoto Y, et al. Characterization of leukocyte mono-immunoglobulin-like receptor 7 (LMIR7)/CLM-3 as an activating receptor: its similarities to and differences from LMIR4/CLM-5. *J Biol Chem.* 2010; 285(46):35274–35283.
42. Ono R, et al. Dimerization of MLL fusion proteins and FLT3 activation synergize to induce multiple-lineage leukemogenesis. *J Clin Invest.* 2005; 115(4):919–929.
43. Kimura H, Hayashi-Takanaka Y, Goto Y, Takizawa N, Nozaki N. The organization of histone H3 modifications as revealed by a panel of specific monoclonal antibodies. *Cell Struct Funct.* 2008; 33(1):61–73.
44. Nozawa RS, et al. Human POGZ modulates dissociation of HP1alpha from mitotic chromosome arms through Aurora B activation. *Nat Cell Biol.* 2010; 12(7):719–727.
45. Tanaka S, et al. Ezh2 augments leukemogenicity by reinforcing differentiation blockage in acute myeloid leukemia. *Blood.* 2012;120(5):1107–1117.
46. Kato N, et al. Two types of C/EBPα mutations play distinct but collaborative roles in leukemogenesis: lessons from clinical data and BMT models. *Blood.* 2011; 117(1):221–233.
47. Piazza F, Valens J, Lagasse E, Schindler C. Myeloid differentiation of FdCP1 cells is dependent on Stat5 processing. *Blood.* 2000; 96(4):1358–1365.

Author's Choice

THE JOURNAL OF BIOLOGICAL CHEMISTRY VOL. 288, NO. 15, pp. 10849–10859, April 12, 2013

Neutral Sphingomyelinase 2 (nSMase2)-dependent Exosomal Transfer of Angiogenic MicroRNAs Regulate Cancer Cell Metastasis*[S]

Received for publication, December 18, 2012, and in revised form, February 18, 2013 Published, JBC Papers in Press, February 25, 2013, DOI 10.1074/jbc.M112.446831

Nobuyoshi Kosaka[‡], Haruhisa Iguchi[‡§], Keitaro Hagiwara[‡¶], Yusuke Yoshioka[‡1], Fumitaka Takeshita[‡], and Takahiro Ochiya[‡2]

From the [‡]Division of Molecular and Cellular Medicine, National Cancer Center Research Institute, 5-1-1, Tsukiji, Chuo-ku, Tokyo 104-0045, Japan, the [§]Pharmacology Research Laboratories, Dainippon Sumitomo Pharma Co., Ltd., 1-98 Kasugadenaka 3-chome, Konohana-ku, Osaka 554-0022, Japan, and the [¶]Department of Biological Information, Graduate School of Bioscience and Biotechnology, Tokyo Institute of Technology, Yokohama, Kanagawa 226-8501, Japan

Background: Contribution of exosomal microRNAs to cancer metastasis remains unknown.
Results: Exosomal angiogenic microRNAs secreted by metastatic cancer cells promote the metastasis through the activation of endothelial cells.
Conclusion: Horizontal transfer of exosomal miRNAs from cancer cells can dictate the microenviromental niche for the benefit of the cancer cell.
Significance: This is the first to connect cancer metastasis to the exosomal microRNA *in vivo*.

The release of humoral factors between cancer cells and the microenvironmental cells is critical for metastasis; however, the roles of secreted miRNAs in non-cell autonomous cancer progression against microenvironmental cells remain largely unknown. Here, we demonstrate that the neutral sphyngomyelinase 2 (nSMase2) regulates exosomal microRNA (miRNA) secretion and promotes angiogenesis within the tumor microenvironment as well as metastasis. We demonstrate a requirement for nSMase2-mediated cancer cell exosomal miRNAs in the regulation of metastasis through the induction of angiogenesis in inoculated tumors. In addition, miR-210, released by metastatic cancer cells, was shown to transport to endothelial cells and suppress the expression of specific target genes, which resulted in enhanced angiogenesis. These findings suggest that the horizontal transfer of exosomal miRNAs from cancer cells can dictate the microenviromental niche for the benefit of the cancer cell, like "on demand system" for cancer cells.

The secretion of humoral factors from cancer cells to microenvironmental cells is essential for metastasis during cancer development (1). Although microRNAs (miRNAs)[3] are known as tumor suppressors of cell autonomous malignancy phenotypes such as metastasis (2) and multidrug resistancy (3), the roles of miRNAs in non-cell autonomous cancer progression against microenvironmental cells remain largely unknown. The existence of secretory RNA has been known for many years (4, 5), and recent reports have shown that miRNAs (6), which regulate various types of biological phenomena through the regulation of a variety of target genes, are secreted from cells via the exosome (7, 8). These findings have raised the possibility that RNAs, including miRNAs, may serve as novel humoral factors in cell-cell communication (9). We recently demonstrated that miRNAs are released through neutral sphingomyelinase 2 (nSMase2)-regulated secretory machinery and that these secretory miRNAs are transferable and functional in recipient cells (10). Furthermore, we also found that a tumor-suppressive miRNA secreted from non-cancerous cells via this pathway could be transported between cells and exert gene silencing in the recipient cancer cells, thereby leading to an inhibition of cancer cell growth (11). In the last few years, it has become clear that exosomal miRNAs play critical roles in mediating cell-cell communication, specifically between immune cells, endothelial cells and cancer cells (12–17). These findings provide evidence that exosomal miRNAs are required for cell-cell communication in various physiological and pathological conditions, although the contribution of extracellular miRNAs to cancer metastasis remains largely unknown (9). Here, we first demonstrated that horizontal transfer of exosomal miR-210 from metastatic cancer cells could dictate the microenvironmental endothelial cells to the benefit of the cancer cells, which contributed to cancer metastasis. Preventing the expression of

* This work was supported in part by a grant-in-aid for the third term comprehensive 10-year strategy for cancer control, a grant-in-aid for scientific research on priority areas cancer from the Ministry of Education, Culture, Sports, Science, and Technology, and the Program for Promotion of Fundamental Studies in Health Sciences of the National Institute of Biomedical Innovation (NiBio), and the Japan Society for the Promotion of Science through the Funding Program for world leading innovative R&D on science and technology (FIRST Program) initiated by the Council for Science and Technology Policy, and a grant-in-aid for Scientific Research on Innovative Areas (functional machinery for non-coding RNAs) from the Japanese Ministry of Education, Culture, Sports, Science, and Technology.
Author's Choice—Final version full access.
[S] This article contains supplemental Figs. 1–9.
[1] A research fellow for the Japan Society for the Promotion of Science.
[2] To whom correspondence should be addressed: Div. of Molecular and Cellular Medicine, National Cancer Center Research Inst., 1-1 Tsukiji, 5-chome, Chuo-ku, Tokyo 104-0045, Japan. Tel.: 81-3-3542-2511 (ext. 4800); Fax: 81-3-5565-0727; E-mail: tochiya@ncc.go.jp.

[3] The abbreviations used are: miRNA, microRNA; nSMase2, neutral sphingomyelinase 2; KD, knockdown; luc, luciferase; HUVEC, human umbilical cord vein endothelial cell; nSMase2-OE, nSMase2-overexpressing cancer cells; qRT-PCR, quantitative RT-PCR.

nSMase2 in metastatic cancer cells abrogates the metastatic ability of cancer cells to target lung tissues, whereas reconstitution via the administration of exosomes isolated from metastatic cancer cells rescued this phenomenon. In this context, the number of endothelial cells in inoculated tumors was proportional to the expression level of nSMase2 in cancer cells. In fact, exosomes derived from a metastatic cancer cell line enhanced the capillary formation and migration of endothelial cells *in vitro*. Interestingly, the expression profiles of exosomal miRNAs obtained from metastatic cancer cells demonstrated that a set of angiogenic miRNAs were highly concentrated in these exosomes. One of them, miR-210, enhanced the angiogenesis through the suppression of specific target gene, which resulted in enhanced angiogenesis. These results revealed that cancer cells provide nSMase2-regulated exosomal miRNAs to endothelial cells to promote their metastatic initiation efficiency.

EXPERIMENTAL PROCEDURES

Reagents—Goat polyclonal anti-Alix (Q-19; sc-49268) and donkey anti-goat IgG (HRP; sc-2020) were purchased from Santa Cruz Biotechnology. Mouse monoclonal anti-HSP70, clone 7/HSP70 (610607), and mouse monoclonal ant-human CD63 antibody (556019) were purchased from BD Biosciences. Rabbit polyclonal anti-CD31 antibody (ab28364) was from Abcam. Peroxidase-labeled anti-mouse antibodies were purchased from GE Healthcare (NA931V). GW4869 was purchased from Calbiochem (Darmstadt, Germany). Geneticin and puromycin were purchased from Invitrogen.

Cell Culture—4T1 cells, a mouse breast cancer cell line, MCF7, non-metastatic breast cancer cells, and MCF10A, normal mammary epithelial cells, were obtained from the American Type Culture Collection (Manassas, VA). MDA-MB-231-D3H1 and MDA-MB-231-D3H2LN, a metastatic human breast cancer cell line, were obtained from Xenogen. 4T1, MCF7, MDA-MB-231-D3H1, and MDA-MB-231-D3H2LN were cultured in RPMI containing 10% heat-inactivated FBS and antibiotic-antimycotic (Invitrogen) at 37 °C in 5% CO_2. Human umbilical cord vein endothelial cells (HUVECs) were purchased from Lonza and cultured in EBM-2 BulletKit (Lonza) supplemented with 2% FBS.

Exosome Purification—Exosomes were purified by differential centrifugation as described previously (10). The exosome fraction was measured for its protein content using the Micro BCA protein assay kit (Thermo Scientific, Wilmington, DE).

Tube Formation Assay—HUVECs (100,000) cells were cultured on 150 μl of Matrigel (Sigma) in culture medium for 16 h in 24-well plate. The degree of tube formation was quantified by measuring the number of branches in five randomly chosen fields from each well using NIH ImageJ software. For rescue experiments, HUVECs were transfected using Dharmafect reagent (Dharmacon) according to the manufacturer's recommendations with anti-control or anti-miR-210 (Ambion). After 24 h of posttransfection, cells were seeded onto Matrigel as described above with 1 μg of exosome.

Establishment of Stable Cell Lines—A stable 4T1 and MDA-MB-231-D3H2LN nSMase2-modified cell lines that expressed mouse nSMase2 shRNA, human nSMase2 shRNA, and pCT-CD63-GFP were generated by selection with puromycin. A stable 4T1 and MDA-MB-231-D3H2LN cell lines that overexpresses human nSMase2 were generated by selection with geneticin. 4T1 cells or MDA-MB-231-D3H2LN were transfected with 0.5 μg of the vector at 90% confluency in 24-well dishes using a Lipofectamine LTX reagent in accordance with the manufacturer's instructions.

Co-culture Experiments—Well inserts for 24-well plates with a 0.4-μm pore-sized filter were purchased from BD and used following the manufacturer's instructions. 4T1 control cells, 4T1-nSMase2-KD cells, 4T1-siLuc cells, or 4T1-CD63-GFP cells (100, 000) were seeded into the well inserts. HUVECs (200, 000) were seeded into 24-well plates.

Confocal Microscopy—Confocal microscopy was done on an Olympus laser scanning microscope FV10i (Olympus). Filters used were 489–510 nm (GFP and Alexa Fluor 488) and 577–603 nm (Alexa Fluor 568).

Immunoblot Analysis—Exosomes were lysed in a 2% SDS buffer, and equal amounts of protein were loaded onto an SDS-PAGE gel. Anti-Alix (1:200), anti-HSP70 (1:1,000), and anti-CD63 (1:200) were used as primary antibodies. The dilution ratio of each antibody is indicated in *parentheses*. Two secondary antibodies (peroxidase-labeled anti-goat and anti-mouse antibodies) were used at a dilution of 1:2000. Bound antibodies were visualized by chemiluminescence using the ImmunoStar LD (290-69904) (Wako), and luminescent images were analyzed by a LuminoImager (LAS-3000; Fujifilm, Inc.). Only gels for CD63 (BD Biosciences) detection were run under non-reducing conditions.

Plasmids—psiRNA-LucGL3 was purchased from InvivoGen. Knockdown shRNA vector for human and mouse nSMase2 were purchased from TaKaRa Bio. A full-length human nSMase2 cDNA was cloned into pIRES2-EGFP vector (Clontech). Primary miR-210 were PCR-amplified from human genomic DNA and cloned into the downstream of CMV promoter in pIREShyg3 (Takara Bio). The sensor vector for miR-210 was constructed by introducing tandem binding sites with perfect complementarity to miR-210, separated by a four-nucleotide spacer into the XhoI site of psiCHECK2 (Promega). The sequences of the binding site are as follows: 5′-TTCTCGAGTTTCAGCCG-CTGTCACACGCACAGTTACGCGTTTTCAGCCGCTGT-CACACGCACAGTTCTCGAGTT-3′ (sense) and 5′-AACTC-GAGAACTGTGCGTGTGACAGCGGCTGAAAACGCGT-AACTGTGCGTGTGACAGCGGCTGAAACTCGAGAA-3′ (antisense). The "seed" sequence of miR-210 is *underlined*. In a mutated miR-210 sensor vector, the seed sequence, ACACGCA, was displaced with TGTGCGT. All of the plasmids were verified by DNA sequencing.

Isolation of RNAs—Isolation of exosomal and cellular RNAs was performed using the miRNeasy Mini Kit (Qiagen). Exosome or cell lysate was diluted with 1 ml of Qiazol solution. Subsequent extraction and filter cartridge work were carried out according to the manufacturer's protocol.

mRNA and miRNA Expression Analysis—The method for qRT-PCR has been described previously (10). PCR was carried out in 96-well plates using the 7300 Real Time PCR system (Applied Biosystems). All reactions were done in triplicate. All TaqMan MicroRNA assays were purchased from Applied Bio-

systems. RNU6 was used as an invariant control for the cells. Gene expression was analyzed using Taqman gene expression assays except primary miR-210 (Applied Biosystems). The expression levels of primary miR-210 and β-actin were measured by qRT-PCR using a SYBR Green PCR Master Mix (Invitrogen). Primer sequences are as follows (shown 5′ to 3′): primary miRNA-210, GACTGGCCTTTGGAAGCTCC (forward) and ACAGCCTTTCTCAGGTGCAG (reverse); β-actin, GGCACCACCATGTACCCTG (forward) and CACGGAGTACTTGCGCTCAG (reverse).

Nanoparticle Tracking Analysis—Nanoparticle tracking analysis was carried out using the Nanosight LM10-HS system (NanoSight) on exosomes resuspended in PBS and were further diluted for analysis. The results are presented as the average ± S.E. of three independent experiments.

Phase Contrast Electron Microscopy—A drop of the sample was put on a copper grid and coated with a carbon film with holes in it. Most of the liquid was removed with blotting paper, leaving a thin film stretched over the holes. The specimen was instantly shock-frozen by plunging into liquid ethane, which was cooled to 90 K by liquid nitrogen into a temperature-controlled freezing unit (Zeiss, Oberkochen, Germany). The remaining ethane was removed with blotting paper, and the specimen was transferred to the electron microscope. The phase plate was prepared from amorphous carbon films. The films were deposited by vacuum evaporation (JEOL JEE-400) on a freshly cleaved mica surface. For observation at 300-kV acceleration voltage, the film thickness corresponding to the *p*/two-phase plate was approximately 32 nm. At that thickness, the transparency of 300-kV acceleration electrons was estimated to be 70%. After preparation, the films were floated on the water's surface and then transferred to a molybdenum aperture with several holes 50-lm in diameter, which resulted in a cut-off frequency for special resolution of 0.5 nm. A hole approximately 0.5 lm in diameter in the center of the carbon film was used by a focused ion beam machine (JEOL JFIB-2000).

PKH67-labeled Exosome Transfer—Purified exosomes derived from 4T1 conditioned medium were labeled with a PKH67 green fluorescent labeling kit (Sigma-Aldrich). Exosomes were incubated with 2 μM PKH67 for 5 min, washed four times using 100-kDa filter (Microcon YM-100, Millipore) to remove excess dye, and incubated with HUVECs at 37 °C.

Microarray Analysis—To detect the miRNAs in exosomes and cells derived from HEK293, MCF10A, MCF7, and MDA-MB-231, 100 ng of total RNA was labeled and hybridized using a human microRNA microarray kit (Agilent Technologies) according to the manufacturer's protocol (protocol for use with Agilent MicroRNA microarrays, version 1.5). Hybridization signals were detected using a DNA microarray scanner (Agilent Technologies), and the scanned images were analyzed using Agilent Feature Extraction software.

Mouse Studies—Animal experiments in this study were performed in compliance with the guidelines of the Institute for Laboratory Animal Research, National Cancer Center Research Institute. Five- to seven-week-old female Balb/c athymic nude mice (CLEA Japan, Shizuoka, Japan) or SCID Hairless Outbred mice (Charles River Laboratories, Kanagawa, Japan) were anesthetized by exposure to 3% isoflurane for injections and *in vivo* imaging. We injected 4T1- or MDA-MB-231-D3H2LN-nSMase2-modified cells bilaterally into the subcutaneous (2×10^6 cells were injected in 100-μl volume PBS) or mammary fat pad (2×10^6 cells were injected in 50-μl volume Matrigel diluted with PBS) of anesthetized mice. We monitored mammary tumor growth by regular measurements using a digital caliper. After 3 to 4 weeks, we killed mice and determined metastasis in lungs by *ex vivo* or *in vivo* imaging. We carried out lung colonization assays by injecting 1×10^6 4T1-control or 4T1-nSMase2-KD cells (suspended in 100 μl of PBS) into the lateral tail vein. Lung colonization was studied and determined by *in vivo* luminescence imaging. For rescue experiment, 4T1-nSMase2-KD cells (2×10^6 cells suspended in 100 μl of PBS) were subcutaneously injected. After 4 days of implantation, 1 μg of exosome was injected intratumoraly (100 μl in PBS) every other day for up to 18 days. Metastasis occurrence was determined by *in vivo* luminescence. For *in vivo* imaging, the mice were administered D-luciferin (150 mg/kg, Promega) by intraperitoneal injection. Ten minutes later, photons from animal whole bodies were counted using the IVIS imaging system (Xenogen) according to the manufacturer's instructions. Data were analyzed using LIVINGIMAGE software (version 2.50, Xenogen).

Statistics—Statistical analyses were performed using the Student's *t* test.

RESULTS

nSMase2 Regulates Cancer Cell Metastasis—In a previous study, we have described how miRNAs are released through ceramide-dependent secretory machinery via the exosome (10). Specifically, we demonstrated that blocking the activity of nSMase2 resulted in reduced miRNA secretion and that nSMase2 overexpression led to increased levels of extracellular miRNAs (10, 11). In addition, we found that the expression level of nSMase2 was higher in cancer cells than that in non-cancer cells (Fig. 1*A*, *upper panel* and supplemental Fig. 1*A*). Furthermore, secretion level of exosome show correlation with the expression level of nSMase2 (Fig. 1*A*, *lower panel*, and supplemental Fig. 1*B*), suggesting that malignant cancer cells secrete more exosomes than non-cancer cells through the regulation of nSMase2. We confirmed that breast cancer cells secreted around 100-nm size of vesicles with a consistent size and uniform expression of known exosome marker, CD63 and HP70 (supplemental Fig. 1*C*) (18). Purified exosomes has also been shown by phase contrast electron microscopy and found that their size observed to be 90 ± 11.7 nm in diameter ($n = 13$) (Fig. 1*B*). To determine the role of nSMase2 in cancer cell malignancy, we employed 4T1 cells, which are mouse mammary tumor cells with a high tumorigenic and metastatic ability. Both stable nSMase2-knockdown and nSMase2-overexpressing 4T1 cells were generated (supplemental Figs. 1, *D* and *E*) and inoculated into mammary fat pad of the mice, and the tumors were subsequently evaluated for their metastatic colonization capacity in lung tissue. The expression of secretory miR-16 (supplemental Fig. 2*A*), which is known to abundantly existed in exosome, as well as exosome quantity, as determined by immunoblotting for exosome markers, HSP70 and Alix (supplemental Fig. 2*B*), protein concentration (supplemental Fig. 2*C*), and nanopar-

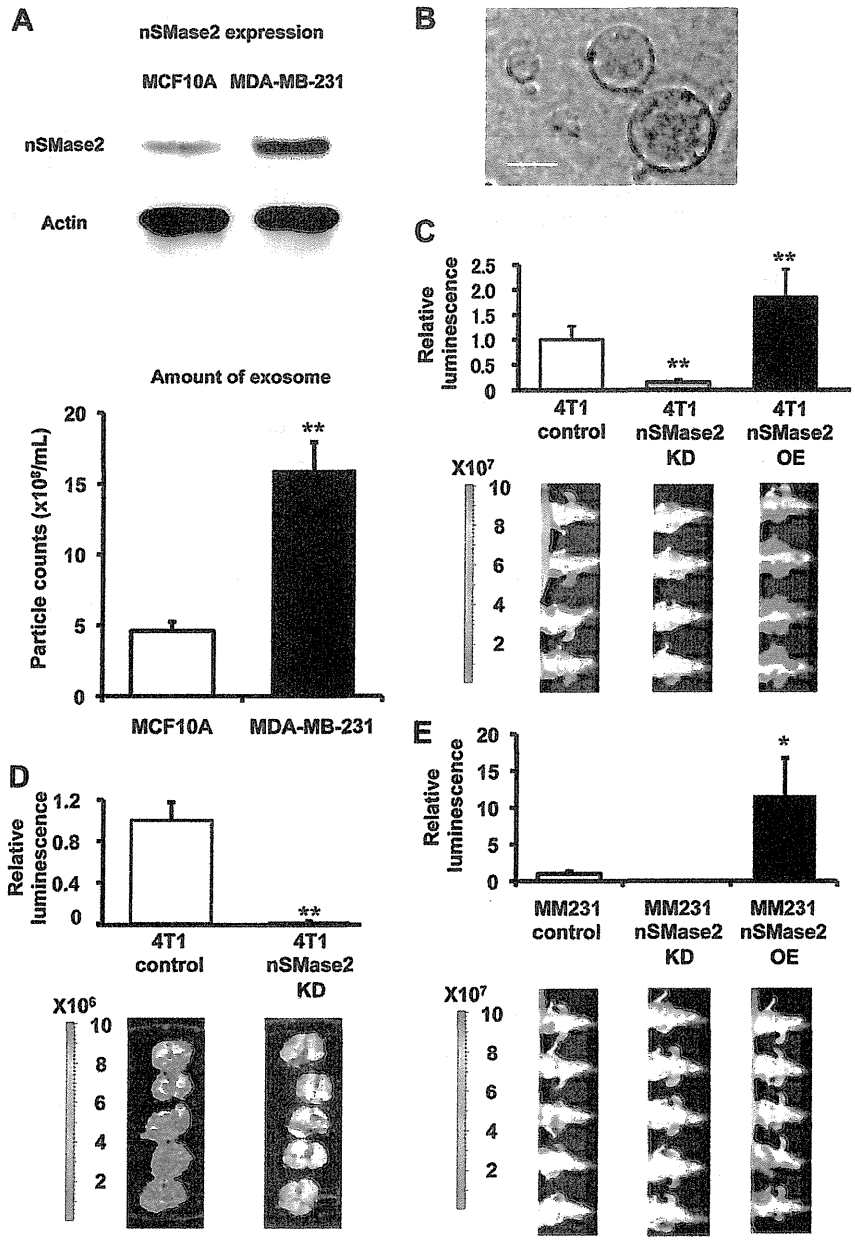

FIGURE 1. **nSMase2 regulates cancer cell metastasis.** *A*, the expression level of nSMase2 protein in (*upper panel*) and secretion level of exosome from (*lower panel*) MCF10A and MDA-MB-231 cells. The same number of cells was seeded. *Error bars* are presented as the mean S.E. ($n = 3$). **, $p < 0.005$, as compared with MCF10A cells. *B*, phase-contrast electron microscopy was used to image resuspend exosome pellets. *Scale bar*, 100 nm. *C*, bioluminescence quantification of lung metastasis by 4T1-control cells, 4T1-nSMase2-KD cells or 4T1-nSMase2-OE cells. Each *error bar* is presented as the mean S.E. ($n = 4$). **, $p < 0.005$, as compared with 4T1-control cells. *D*, luciferase activity in the lung, which was used to represent lung metastasis, was recorded for each mouse. Lung images from different mice are shown. Each *error bar* is presented as the mean S.E. ($n = 5$). **, $p < 0.005$, as compared with 4T1-control cells. *E*, bioluminescence quantification of metastasis by parental MDA-MB-231-D3H2LN (*MM231-control*) cells, MDA-MB-231-D3H2LN-nSMase2-OE (*MM231-nSMase2-OE*) cells, or MDA-MB-231-D3H2LN-nSMase2-KD (*MM231-nSMase2-KD*) cells. Each *error bar* is presented as the mean ± S.E. ($n = 5$). *, $p < 0.05$, as compared with MM231-control cells.

ticle tracking analysis (supplemental Fig. 2*D*), decreased in nSMase2-knockdown cancer cells (4T1-nSMase2-KD cells) but increased in nSMase2-overexpressing cancer cells (4T1-nSMase2-OE cells). However, the expression of intracellular miRNAs was not altered in either of these established cell types (supplemental Figs. 2*A* and 3). After the orthotopic inoculation of these cell lines into mammary fat pad, we found that nSMase2 silencing in parental 4T1 breast cancer cells significantly decreased lung metastatic colonization (Fig. 1*C*), and *in vivo* imaging and histological observation revealed a significant decrease in the total number of metastatic nodules in nSMase2-knockdown lung tumors (Fig. 1*D* and supplemental Fig. 4*A*). In contrast, the overexpression of nSMase2 in 4T1 cells enhanced the metastatic capacity of these tumors (Fig. 1*C*). We also confirmed similar results using an orthotopic model of MDA-MB-231-D3H2LN cells, which are human breast cancer cells with a

high metastatic ability, overexpressing or inhibiting nSMase2 (Fig. 1*E*), which suggests that the alteration in expression level of nSMase2 leads to the change in metastatic ability of cancer cells. Interestingly, nSMase2 inhibition or overexpression in 4T1 cells did not significantly enhance or inhibit cellular proliferation, invasion, or migration *in vitro* (supplemental Fig. 4*B*) and did not increase the mammary tumor volume (supplemental Fig. 4, *C* and *D*). In addition, no significant differences were found in expression profiles of cellular or miRNAs isolated from these nSMase2-modified cell lines (supplemental Fig. 3). Moreover, no significant reduction in metastatic potential was observed in the lungs of animals intravenously injected with parental 4T1 cells or 4T1-nSMase2-KD cells, which excludes the possibility that nSMase2 disruption affected the recruitment capacity of cancer cells to metastatic tissues (supplemental Fig. 5). These results indicate that the effect of nSMase2 on metastasis was not simply due to its effect on the cancer cells themselves.

Endothelial Activation Regulated by nSMase2-mediated Exosome Promotes Cancer Cell Metastasis—Consistent with a role for nSMase2 in the initiation of metastasis, intratumor injection of exosomes isolated from parental 4T1 cells to non-metastatic 4T1-nSMase2-KD cells after orthotopical inoculation into mammary fat pad significantly enhanced their metastatic colonization (Fig. 2*A* and supplemental Fig. 6*A*), whereas the growth of the inoculated 4T1-nSMase2-KD tumor cells was unaffected (supplemental Fig. 6*B*). These results indicated that endogenous nSMase2 could act to enhance metastatic initiation through the secretion of exosomes. When examining the selective disadvantage provided by nSMase2 silencing in cancer cells, we noticed that blood vessels were difficult to detect in animals that received 4T1-nSMase2-KD cells (Fig. 2*B*, *left panel*). As a result, we hypothesized that tumors inoculated with nSMase2-knockdown cells would display reduced blood vessel densities upon microscopic visualization of the primary tumor after staining for the endothelial marker CD31. The imaging analysis revealed that primary tumors derived from 4T1-nSMase2-KD cells had significantly lower endothelial cell densities than did tumors derived from control cells (Fig. 2*B*, *right panel*, and 2*C*). In contrast, tumors derived from 4T1-nSMase2-OE cells displayed higher endothelial densities than did tumors derived from control cells (Fig. 2*B*, *right panel*, and 2*C*). In addition, there were increased numbers of endothelial cells in tumors derived from 4T1-nSMase2-KD cells that were subsequently injected with parental 4T1 cell-derived exosomes compared with control treatment (Fig. 2, *D* and *E*). Thus, these observations indicate that release of nSMase2-mediated exosome enhances endothelial cell density, whereas the inhibition of nSMase2 provides metastatic cells with a selective disadvantage for endothelial interactions and angiogenic progression.

Exosomes Derived from Metastatic Cancer Cells Enhances Activity of Endothelial Cells—We next sought to determine the cellular basis for nSMase2-regulated exosome-dependent angiogenesis. For this purpose, we first evaluated the effect of exosome from parental 4T1 cells in HUVECs. As a result, although cellular proliferation of HUVECs was slightly increased by the addition of 4T1 exosome (supplemental Fig. 7*A*), addition of purified exosomes derived from metastatic 4T1 cells enhanced not only tube formation in HUVECs, as assessed by the quantification of branch points (Fig. 3*A*), but also migration of HUVECs (Fig. 3*B*). Next, to determine whether exosomes secreted by metastatic breast cancer cells could be incorporated in a paracrine manner, we employed a co-culture system for HUVECs and 4T1 cells, in which the cells are separated by a membrane with a 0.4-μm pore size to prevent direct cell contact or the transfer of larger vesicles. In this experiment, we used 4T1 cells that had been transduced with a CD63-GFP fusion gene, and we analyzed GFP fluorescence present in HUVECs after 3 days of co-culture by confocal microscopy. These studies showed that exosomes could be transferred from breast cancer cells to endothelial cells during co-culture (Fig. 3*C*, *left panel*). However, the transfer of exosomes from cancer cells to endothelial cells was completely abolished by the addition of nSMase2 inhibitor, GW4869 that was reported to inhibit the secretion of exosome from cells (10, 19), to the 4T1-CD63-GFP cells (Fig. 3*C*: right panel). In addition, 4T1 exosomes labeled with the fluorescent dye PKH67 were cultured with HUVECs and were found to be internalized into endosome-like structures by endothelial cells (supplemental Fig. 7*B*). To confirm whether the exosomes from inoculated cancer cells were incorporated into endothelial cells *in vivo*, an immunohistochemical analysis was performed following the inoculation of 4T1-hCD63 cells *in vivo* (Fig. 3*D*). As shown in Fig. 3*D*, the CD31-positive cells (*green*) was co-localized with CD63 (*red*) signals in the tumor. These findings reveal that enhanced tube formation in endothelial cells is a key feature of metastatic breast cancer cell populations that is regulated in a humoral fashion by exosomes released from metastatic cancer cells.

Exosomal Angiogenic miRNAs from Cancer Cells Regulate Angiogenesis in Endothelial Cells—It is well known that angiogenic miRNAs regulate multiple endothelial cell functions and that nSMase2 is essential for miRNA secretion from cells (10, 20, 21). These reports, in addition to our findings described above, prompted us to evaluate the hypothesis that exosomal miRNAs from cancer cells are responsible for this phenomenon. To prove this hypothesis, we used 4T1 cells that had been transduced with a luciferase short hairpin RNA-overexpressing vector (4T1-siLuc). This established cell line secretes luciferase siRNA molecules with a nucleic acid sequence not present in the mammalian genome (supplemental Fig. 8*A*). To evaluate whether the transfer of luciferase siRNA occurred in the form of exosome transfer, we added GW4869 to co-cultured 4T1-siLuc cells and assessed the transfer of luciferase siRNA to HUVECs by qRT-PCR. Although we were able to measure luciferase siRNA in control-treated HUVECs, this siRNA sequence was minimally detected in HUVECs co-cultured with GW4869 treated 4T1-siLuc cells (Fig. 4*A*), which indicates that small RNAs, including not only siRNA but also miRNA, could in fact be transferred from cancer cells to endothelial cells during co-culture and that the transfer of small RNAs is mediated by exosome release regulated by nSMase2. We next sought to determine whether exosomal miRNAs could selectively regulate the angiogenesis of endothelial cells. To address this hypothesis, we performed a miRNA microarray analysis of the following four cell lines: metastatic breast cancer cells (MDA-MB-231); non-metastatic cancer cells (MCF7); normal mam-

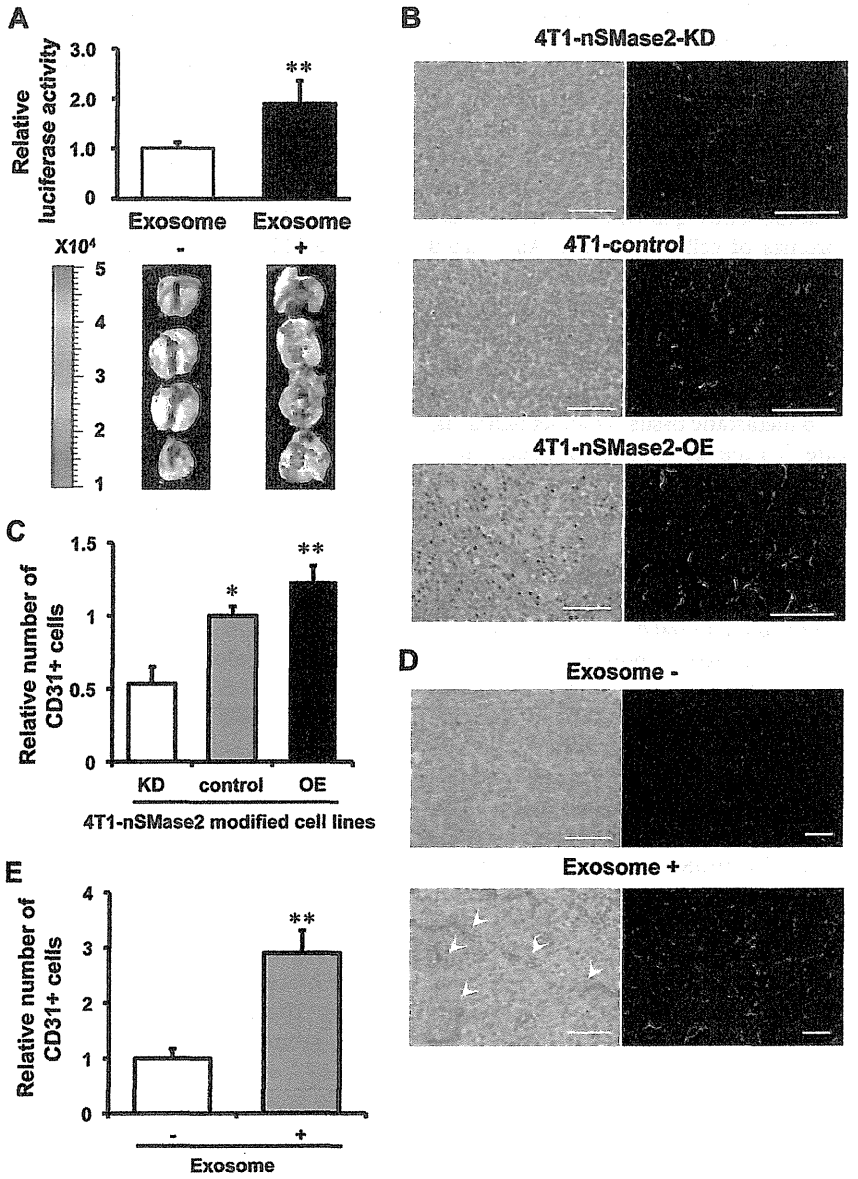

FIGURE 2. **Endothelial activation mediated by nSMase2 regulates cancer cell metastasis.** *A*, bioluminescence imaging of lung metastasis by 4T1-nSMase2-KD cells with or without the injection of exosomes isolated from parental 4T1 cells. Each *error bar* is presented as the mean ± S.E. ($n = 4$). **, $p < 0.005$, as compared with control injection. *B*, H&E of primary tumors isolated from parental 4T1-control cells, 4T1-nSMase2-KD cells or 4T1-nSMase2-OE cells (*left panel*). *Scale bars*, 100 μm for H&E. The endothelial cells were also evaluated using CD31 staining to detect blood vessels in tumors composed of parental 4T1 cells, 4T1-nSMase2-KD cells or 4T1-nSMase2-OE cells (*right panel*); *scale bars*, 100 μm. *C*, angiogenesis determined using CD31 staining which shown in *B* to detect blood vessels in tumors composed of parental 4T1 cells, 4T1-nSMase2-KD cells, or 4T1-nSMase2-OE cells, as above; $n = 4$ for each group. Each *error bar* is presented as the mean ± S.E. ($n = 4$). *, $p < 0.05$; **, $p < 0.005$, as compared with 4T1 control. *D*, H&E staining of primary tumors isolated from mice that received PBS or an injection of exosomes from parental 4T1 cells following the transplantation of 4T1-nSMase2-KD cells (*left panel*). *Arrowheads* show red blood cells in vascular structure. *Scale bars*, 100 μm for H&E. The endothelial cells were also evaluated using CD31 staining to detect blood vessels in tumors composed of 4T1-nSMase2-KD cells with or without exosome injection (*right panel*); *scale bars*, 200 μm. *E*, angiogenesis determined using CD31 staining, which was shown in *D* to detect blood vessels in tumors composed of 4T1-nSMase2-KD cells with or without exosome, as above; $n = 4$ for each group. Each *error bar* is presented as the mean ± S.E. ($n = 4$). **, $p < 0.005$, as compared with control injection.

mary epithelial cells (MCF10A); and human embryonic kidney cells (HEK293). The microarray analysis of miRNA populations in exosomes isolated from these cell lines were performed using a miRNA microarray (Fig. 4*B*). Interestingly, some of the exosomal miRNAs that were highly enriched in the metastatic cancer cell line are known to regulate angiogenesis in endothelial cells (22). One of these miRNAs, miR-210, which is well known as an angiogenic miRNA, and its expression was correlated with poor prognosis in breast cancer (23, 24). Moreover, a recent report showed that high expression levels of miR-210 in plasma are associated with the presence of tumor in patients with breast cancer and with trastuzumab resistance in patients with HER2-positive breast cancer (25). In addition, the expression level of miR-210 was significantly higher in breast cancer patients with lymph node metastasis than in breast cancer patients without lymph node metastasis (25). From our data

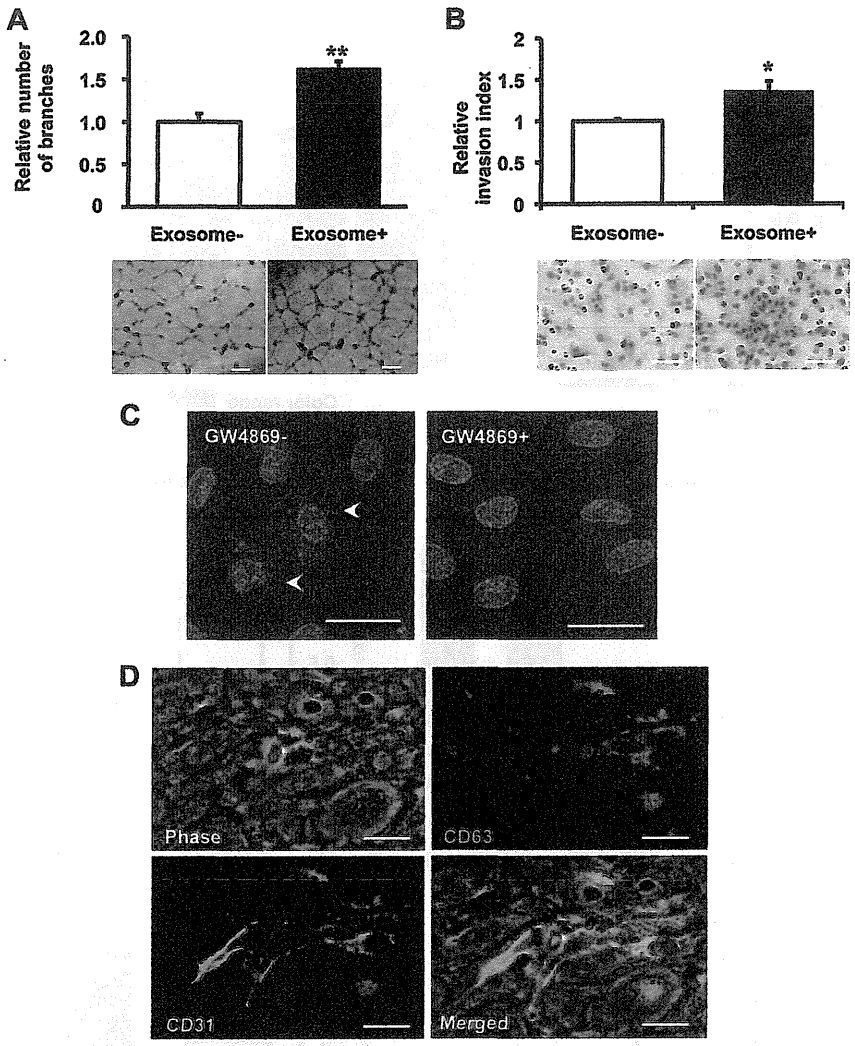

FIGURE 3. **Exosomes derived from metastatic cancer cells enhances activity of endothelial cells.** *A*, capillary tube formation in endothelial cells seeded onto Matrigel following the addition of exosomes from parental 4T1 cells. A representative image at 16 h after plating is shown, including the quantification of the average number of branches at 16 h after plating. The *scale bar* indicates 500 μm. *B*, the effect of exosome on HUVEC migration was determined by Transwell migration assay. A representative image at 48 h after plating is shown, including the quantification of the average number of migrated HUVECs at 48 h after plating. The *scale bar* indicates 100 μm. *C*, an *in vitro* co-culture system was used, whereby 4T1 cells were seeded in the *top compartment* and separated from HUVECs in the *bottom compartment* by a porous membrane. 4T1 cells (*top compartment*) were transduced with a CD63-GFP vector and co-cultured with HUVECs (*bottom compartment*). *Scale bars*, 100 μm. *D*, immunostaining of CD31 (*green*) and CD63 (*red*) on 4T1-hCD63 inoculated tumor. The *scale bar* indicates 10 μm. CD63 is co-localized with CD31-positive endothelial cells.

and previous reports, because the contribution of exosome against cancer metastasis was mediator of endothelial activation, we postulated that exosomal miR-210 might be one of the regulators in exosome for the angiogenesis around the cancer cells. Indeed, miR-210 expression in exosome was higher in malignant cancer cells than that in non-malignant cancer cell or non-cancer cells (Fig. 4*C*). To confirm that exosomal miR-210 were down-regulated in nSMase2-impaired cancer cells, we performed a qRT-PCR analysis for these cells. As shown in Fig. 4*D*, the expression of exosomal miR-210 was down-regulated in nSMase2 knockdown cells when compared with control cells, although the cellular levels of the miRNAs were not altered (supplemental Fig. 8*B*). Moreover, we performed a co-culture experiment using 4T1-nSMase-KD cells or parental 4T1 cells with HUVECs and then measured the expression of miR-210 in the HUVECs. Co-culture with parental 4T1 cells, compared with 4T1-nSMase-KD cells, led to the higher detection of miR-210 in HUVECs (Fig. 4*E*), indicating that exosomal miR-210 from metastatic cancer cells transfer to recipient endothelial cells. Then, we employed this co-culture system to study the effects of exosomes isolated from parental 4T1 cells on the expression of the established miR-210 target gene, ephrin-A3 (26). The presence of parental 4T1 cells reduced the expression level of ephrin-A3 in HUVECs compared with 4T1-nSMase2-KD cells (Fig. 4*F*). To exclude the possibility that the exosome from cancer cells itself induces the endogenous expression of miR-210 in HUVECs, we quantified the expression of primary miR-210 in HUVECs co-cultured with parental 4T1 cells or 4T1-nSMase-KD cells. As shown in supplemental Fig. 8*C*, we did not find any difference of primary miR-210

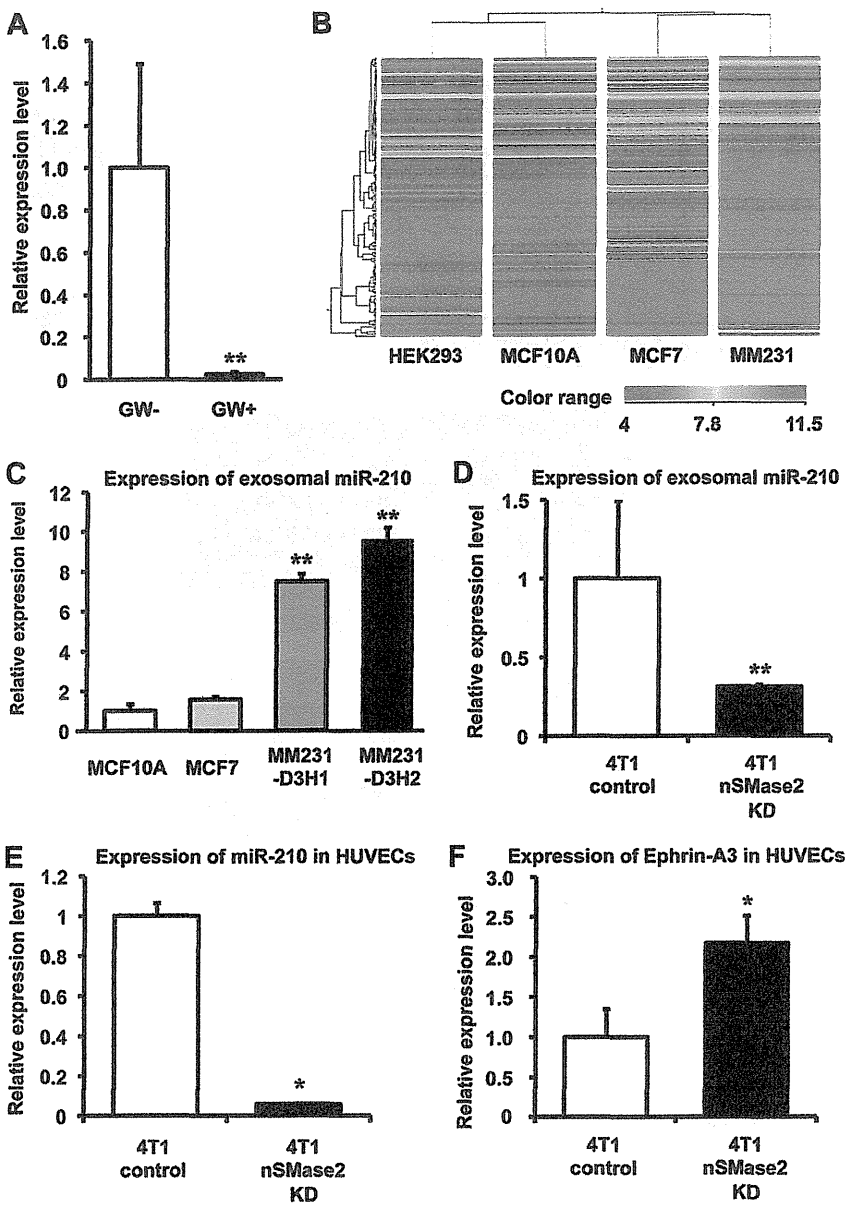

FIGURE 4. **Exosomal angiogenic miRNAs from cancer cells regulate angiogenesis in endothelial cells.** *A*, 4T1-siLuc cells were treated with 10 μM GW4869 at the start of the co-culture for a total of 48 h ($p < 0.001$). Each *error bar* is presented as the mean ± S.E. ($n = 3$). **, $p < 0.005$, as compared with control. *B*, heat map showing expression levels of the exosomal miRNAs isolated from HEK293, MCF10A, MCF7, and MDA-MB-231. *Blue* to *red*, color range gradient of mean abundance. *C*, the expression level of miR-210 in exosome isolated from MCF10A, MCF7, MDA-MB-231-D3H1 (MM231-D3H1), or MDA-MB-231-D3H2LN (MM231-D3H2) cells. Each *error bar* is presented as the mean ± S.E. ($n = 3$). **, $p < 0.005$, as compared with MCF10A. *D*, expression of exosomal miR-210 in exosomes isolated from parental 4T1 cells or 4T1-nSMase2-KD cells. Each *error bar* is presented as the mean ± S.E. ($n = 4$). **, $p < 0.005$, as compared with 4T1-control cells. *E*, HUVECs were co-cultured with parental 4T1 cells or 4T1-nSMase2-KD cells for 48 h. RNA was isolated from the HUVECs at 48 h after the start of co-culture, and the expression of exosomal miR-210 in the HUVECs was analyzed by qRT-PCR. Each *error bar* is presented as the mean ± S.E. ($n = 3$). *, $p < 0.05$, as compared with 4T1 control cells. *F*, parental 4T1 cells or 4T1-nSMase2-KD cells were co-cultured with HUVECs for 48 h, and the expression levels of ephrin-A3 (target of miR-210) were analyzed by qRT-PCR. Each *error bar* is presented as the mean ± S.E. ($n = 3$). *, $p < 0.05$, as compared with 4T1-control cells.

expression level between HUVECs co-cultured with parental 4T1 cells or 4T1-nSMase-KD cells, although the expression of primary miR-210 levels was induced 20-fold above basal levels by desferrioxamine, which is an iron chelator and known to induce the expression of hypoxia inducible factor-1α (27), treatment compared with untreated cells (supplemental Fig. 8*D*). Taken together, these results suggest that the enhanced angiogenesis mediated by exosomes isolated from metastatic cancer cells is due to the presence of angiogenic miRNAs within the exosomes.

Exosomal miR-210 Enhanced Angiogenic Activity in Endothelial Cells in Vitro—To show the direct evidence that exosomal miR-210 released from cancer cells contributed to the enhancement of endothelial function in HUVECs, we collected miR-210 enriched exosome, which was isolated from miR-210 transiently transfected 4T1 cells. After the transfection of miR-210

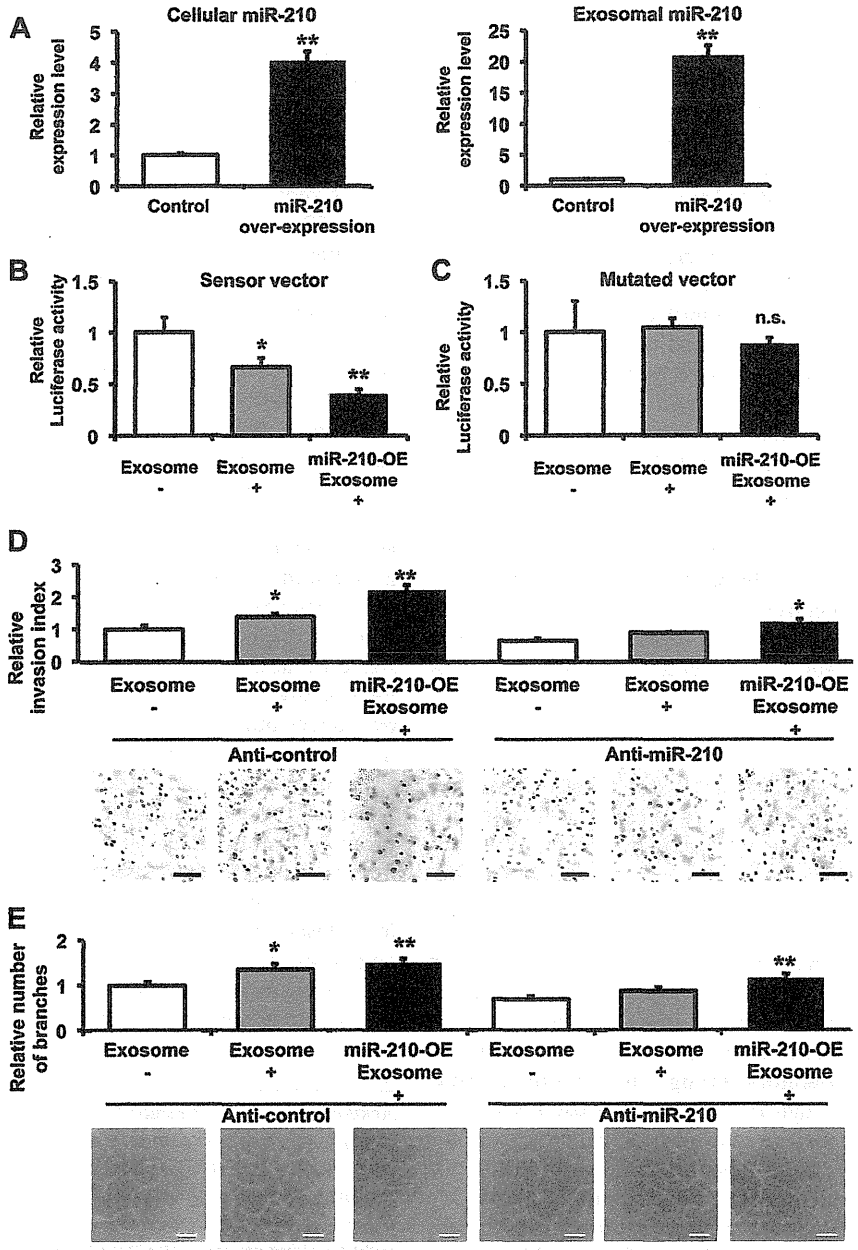

FIGURE 5. **Exosomal miR-210 from cancer cells enhanced the angiogenesis in endothelial cells.** *A*, the expression level of miR-210 in the cells (*left panel*) and exosome (*right panel*) from miR-210 overexpressing cells and control vector transfected cells. Each *error bar* is presented as the mean ± S.E. ($n = 3$). **, $p < 0.005$, as compared with control. *B*, Exosome derived from 4T1 cells suppressed the luciferase activity of the sensor vector. HUVECs transfected with an miR-210 sensor vector were used as recipient cells. The recipient cells were incubated in an miR-210-enriched exosome, control exosome, or PBS. After a 1-day incubation, a luciferase reporter assay was performed. The values on the *y* axis are depicted relative to the normalized luciferase activity of control PBS-treated cells, which is defined as 1. Each *error bar* is presented as the mean ± S.E. ($n = 5$). *, $p < 0.05$; **, $p < 0.005$, as compared with control. *C*, exosome did not reduce the luciferase activity of the mutated sensor vector. HUVECs transfected with the mutated miR-210 sensor vector were used as recipient cells. The recipient cells were incubated in an miR-210-enriched exosome, control exosome, or PBS. The luciferase assay was carried out as described above. The values on the *y* axis are depicted relative to the normalized *Renilla* luciferase activity of control cells, which is defined as 1. Each *error bar* is presented as the mean ± S.E. ($n = 4$). *n.s.* represents not significant. *D*, the transfection of anti-miR-210 to HUVECs inhibited the induction of capillary formation by exosomes derived from 4T1 cells. Following transfection with 3 nM of the miR-210 inhibitory molecule (anti-miR-210) or a control molecule (anti-NC), the HUVECs were incubated for 1 day, and these cells were then assessed using the migration assay with miR-210-enriched exosomes, control exosomes, or PBS. A representative image at 48 h after plating is shown, including the quantification of the average number of migrated HUVECs at 48 h after plating. Each *error bar* is presented as the mean ± S.E. ($n = 3$). *, $p < 0.05$; **, $p < 0.005$ as compared with PBS treatment. The *scale bar* indicates 100 μm. *E*, capillary tube formation in endothelial cells seeded onto Matrigel following the addition of miR-210-enriched exosomes, control exosomes, or PBS. A representative image at 16 h after plating is shown, including the quantification of the average number of branches at 16 h after plating. Each *error bar* is presented as the mean ± S.E. ($n = 3$). *, $p < 0.05$; **, $p < 0.005$ as compared with PBS treatment. The *error bar* indicates 500 μm.

expression vector to 4T1 cells, its expression was increased not only in the cells (Fig. 5*A*, *left panel*) but also in the exosomes (Fig. 5*A*, *right panel*). To confirm whether the transferred miR-210 are functional in the recipient HUVECs or not, we performed an miRNA-responsive reporter assay. We implemented luciferase analyses using a sensor vector harboring *Renilla*